ISPRS Journal of Photogrammetry and Remote Sensing 124 (2017) 89–105

Contents lists available at ScienceDirect

ISPRS Journal of Photogrammetry and Remote Sensing

journal homepage: www.elsevier.com/locate/isprsjprs

Quantifying annual changes in built-up area in complex urban-rural landscapes from analyses of PALSAR and Landsat images

Yuanwei Qin [a], Xiangming Xiao [a,b,*], Jinwei Dong [a], Bangqian Chen [b,c], Fang Liu [d], Geli Zhang [a], Yao Zhang [a], Jie Wang [a], Xiaocui Wu [a]

[a] Department of Microbiology and Plant Biology, Center for Spatial Analysis, University of Oklahoma, Norman, OK 73019, USA
[b] Ministry of Education Key Laboratory of Biodiversity Science and Ecological Engineering, Institute of Biodiversity Science, Fudan University, Shanghai 200433, China
[c] Rubber Research Institute (RRI), Chinese Academy of Tropical Agricultural Sciences, Danzhou City (CATAS), Danzhou Investigation & Experiment Station of Tropical Cops, Ministry of Agriculture, Hainan 571737, China
[d] Institute of Geographic Sciences and Natural Resources Research, Chinese Academy of Sciences, Beijing 100101, China

ARTICLE INFO

Article history:
Received 25 August 2016
Received in revised form 21 November 2016
Accepted 26 December 2016

Keywords:
Built-up
Impervious surface
Urban-rural area
Landsat
PALSAR
Shanghai

ABSTRACT

Built-up area supports human settlements and activities, and its spatial distribution and temporal dynamics have significant impacts on ecosystem services and global environment change. To date, most of urban remote sensing has generated the maps of impervious surfaces, and limited effort has been made to explicitly identify the area, location and density of built-up in the complex and fragmented landscapes based on the freely available datasets. In this study, we took the lower Yangtze River Delta (Landsat Path/Row: 118/038), China, where extensive urbanization and industrialization have occurred, as a case study site. We analyzed the structure and optical features of typical land cover types from (1) the HH and HV gamma-naught imagery from the Advanced Land Observation Satellite (ALOS) Phased Array type L-band Synthetic Aperture Radar (PALSAR), and (2) time series Landsat imagery. We proposed a pixel- and rule-based decision tree approach to identify and map built-up area at 30-m resolution from 2007 to 2010, using PALSAR HH gamma-naught and Landsat annual maximum Normalized Difference Vegetation Index ($NDVI_{max}$). The accuracy assessment showed that the resultant annual maps of built-up had relatively high user (87–93%) and producer accuracies (91–95%) from 2007 to 2010. The built-up area was 2805 km^2 in 2010, about 16% of the total land area of the study site. The annual maps of built-up in 2007–2010 show relatively small changes in the urban core regions, but large outward expansion along the peri-urban regions. The average annual increase of built-up ~~areas~~ was about 80 km^2 per year from 2007 to 2010. Our annual maps of built-up in the lower Yangtze River Delta clearly complement the existing maps of impervious surfaces in the region. This study provides a promising new approach to identify and map built-up area, which is critical to investigate the interactions between human activities and ecosystem services in urban-rural systems.

1. Introduction

Human activities are changing the world's landscapes in pervasive ways to obtain food, fiber, timber and other ecosystem services, and these disturbances alter a series of ecological functions for many ecosystems (DeFries et al., 2004). Artificial impervious surfaces (cities, towns, and settlements) are the most intensive disturbance to natural ecosystems. Although they cover only a small fraction (<1%) of the world's land surface (Schneider et al., 2010), their expansion has a significant impact on regional temperature (Kalnay and Cai, 2003; Weng et al., 2011) and rainfall (Miao et al., 2011; Zhang et al., 2009), biodiversity loss (Guneralp and Seto, 2013; Seto et al., 2012), public health (Gong et al., 2012), and the carbon cycle (Seto et al., 2012).

Remote sensing can map impervious surfaces in the urban areas in a repeat and consistent way (Lu et al., 2014; Weng, 2012). A literature review (Weng, 2012) summarizes the requirement, methods, and trends of remote sensing of impervious surface in the urban areas. Various sensors with different spatial resolutions, spectral resolutions, and temporal resolutions have been used to

* Corresponding author at: Department of Microbiology and Plant Biology, Center for Spatial Analysis, University of Oklahoma, Norman, OK 73019, USA.
E-mail address: xiangming.xiao@ou.edu (X. Xiao).

http://dx.doi.org/10.1016/j.isprsjprs.2016.12.011
0924-2716/

identify and map impervious surfaces. Coarse spatial resolution imagery is usually used for mapping impervious surfaces at regional and global scales, such as the Operational Linescan System (OLS) from the Defense Meteorological Satellite Program (DMSP) images. DMSP/OLS data have been widely employed for impervious surface mapping in the urban areas, as it has the capability to image nighttime light generated by human settlements and a long history of data in the archive (Xie and Weng, 2016; Zhang and Seto, 2011; Zhou et al., 2014). Due to the incompatible problem in time series, DMSP/OLS data were usually calibrated to track the spatio-temporal changes of impervious surface (Liu et al., 2012; Xie and Weng, 2016). Moderate spatial resolution imagery is rich in spectral and temporal information of land surface and also used for mapping impervious surface and its dynamics, such as Moderate Resolution Imaging Spectroradiometer (MODIS) images (Mertes et al., 2015; Schneider et al., 2009, 2010; Schneider et al., 2015). Both coarse and moderate spatial resolution images can track the trend of impervious surface change, while the mixed pixels are a common issue to estimate the area of impervious surface. High spatial resolution imagery is another major data for mapping impervious surface, such as Landsat. As Landsat datasets become freely available to the public, 30-m Landsat imagery is being increasingly used for mapping the expansion of impervious surface in hot-spot areas (Bagan and Yamagata, 2012; Gao et al., 2012; Li et al., 2015; Zhang and Weng, 2016) and at country scale from the 1980s (Kuang et al., 2016; Schneider and Mertes, 2014; Xian and Homer, 2010). High spatial resolution imagery could largely reduce the mixed pixels but have relatively low capability to distinguish the subtypes of impervious surface. Very high spatial resolution imagery (e.g., IKONOS and QuickBird) contains rich spatial information for feature identification of different types of impervious surface (Lu et al., 2011a; Lu and Weng, 2009; Myint et al., 2011). However, these images have limited spectral information and are easy to be affected by the shadows caused by topography or tall buildings (Dare, 2005; Hsieh et al., 2001). Besides, hyperspectral data (e.g., Earth Observing-1) provides the potential to derive detailed information on the nature and properties of different surface materials on the ground, but it also means a difficulty in image processing and a large data redundancy (Weng, 2012). Hyperspectral data may be more effective in extracting endmembers than multispectral imagery, such as the low albedo surface (Weng et al., 2008).

Different approaches were employed to identify and map the impervious surface based on various remote sensing datasets (Table 1). Firstly, visual image interpretation can depict the spatio-temporal patterns of impervious surface based on the single cloud-free image, but it is time-consuming and needs extensive labor force (Kuang et al., 2014, 2016, 2013). Secondly, supervised classification is widely used in the extraction of impervious surface, such as Support Vector Machine (SVM) (Pandey et al., 2013; Zhang et al., 2016), Random Forest (Li et al., 2015; Zhang et al., 2014a; Zhu et al., 2012), Spectral Mixture Analysis (Lu et al., 2011b; Lu and Weng, 2006, 2009; Small, 2005; Weng et al., 2009), and Maximum Likelihood (Lu et al., 2011a; Myint et al., 2011). Supervised image classification clusters pixels into known classes based on training samples and can map certain land cover types with a high accuracy. Thirdly, unsupervised classification relies purely on spectral and statistical information of individual images (Ban et al., 2015; Corbane et al., 2008; Esch et al., 2013; Zhang and Seto, 2011; Zhou et al., 2014). Fourthly, decision tree classification can be applied to different regions and will not be affected by the other pixels, such as thresholding technique (Liu et al., 2012; Zha et al., 2003), Decision Tree C4.5 (Mertes et al., 2015; Schneider et al., 2009, 2010; Schneider and Mertes, 2014; Zhang and Weng, 2016), Decision Tree C5.0 (Gao et al., 2012), and Regression Tree Model (Xian and Homer, 2010). However, the resultant impervious surface maps are easy to be affected by the mixed pixels. Fifthly, object-based classification applies various segmentation to identify object features for impervious surface based on the texture and morphological features from very high spatial resolution images from optical (Hu and Weng, 2011; Myint et al., 2011; Voltersen et al., 2014) and SAR/LiDAR sensors (Esch et al., 2010; Gamba et al., 2011), and even coarse spatial resolution images (Xie and Weng, 2016). The level of scale to segment objects and the thresholds for built-up area identification are not robust and need further assessments in different regions (Myint et al., 2011; Weng, 2012).

However, none of the above-mentioned products explicitly separate built-up from impervious surfaces. In this study, built-up pixels are defined as the areas covered by 50% or more building structure (Li et al., 2015; Schneider et al., 2009, 2010). Built-up areas are the main component of human settlements and the major place for human activities. Accurate maps of built-up are fundamentally important for human settlement design, planning and management, and for investigating how to balance the trade-off between urban development and ecosystem services (Yu et al., 2010). Very high spatial resolution images provide opportunities for identifying the detailed built-up area from SPOT 5 (Pesaresi et al., 2008; Syrris et al., 2015), IKONOS and QuickBird (Pesaresi et al., 2011), QuickBird (Myint et al., 2011; Pesaresi and Gerhardinger, 2011), heterogeneous set of images (Pesaresi et al., 2013), and airborne LiDAR (Singh et al., 2012; Yu et al., 2010) based on textural and morphological features. The broad application of these very high spatial resolution images is challenging at large scales due to the huge amount of data and computations involved as well as data availability issues (Ban et al., 2015). Microwave remote sensing (e.g., synthetic aperture radar, SAR) is independent of weather and day/night and can capture the land cover structure and vegetation biomass. The potential of different SAR datasets (C and X bands) for urban extent mapping was recently explored (Esch et al., 2013, 2010; Gamba et al., 2011; Taubenbock et al., 2011). A recent study reported the use of multi-temporal, dual-polarization ALOS PALSAR images for built-up mapping (Zhang et al., 2011). However, relatively large commission and omission errors exist in their maps, as built-up have similar backscatter characteristics with forests and other land cover types; therefore only radar imagery is not sufficient to identify built-up accurately (Qin et al., 2015). The integration of radar and multispectral optical imagery shows their value for land cover maps. Multispectral optical imagery contains land surface reflectance and radar data can capture the structure features of the land surface. Therefore, the integration use of both radar and multispectral optical imagery could combine complementary information and hold great potential for improving land cover maps, especially for the impervious surfaces (Corbane et al., 2008; Zhang et al., 2014a; Zhu et al., 2012). The synergistic combination of radar and optical imagery reached higher map accuracy than did either radar data only or optical imagery only and significantly improved the impervious surface estimation by reducing the confusions with bare land (Corbane et al., 2008; Zhang et al., 2014a; Zhu et al., 2012).

The objectives of this study are: (1) to develop a new and robust approach that combines ALOS PALSAR and Landsat images in a year to identify and map built-up in urban/rural settings at 30-m spatial resolution; and (2) to apply the pixel-based approach to evaluate the dynamics of built-up over years and generate annual maps of built-up areas at 30-m spatial resolution. We selected the lower Yangtze River Delta, China (Landsat Path/Row: 118/038) as the case study area, where rapid urbanization and industrialization has taken place over the past few decades, and provides an example of the urbanization in China (Liu et al., 2014). Specifically, we used PALSAR and Landsat images to track temporal changes of built-up from 2007 to

Table 1
Literature summary of the data source and approaches for the identification of impervious surface and built-up area.

Land cover	Approach		Coarse resolution (DMSP/OLS)	Medium resolution (MODIS)	High resolution			Very high resolution	
					Landsat-like	SAR	Landsat&SAR	IKONOS/QuickBird/SPOT	SAR or LiDAR
Impervious surface	Image and spatial statistics-based methods	Visual interpretation			Kuang et al. (2014, 2016, 2013)				
		Supervised	Pandey et al. (2013)		Bagan and Yamagata (2012), Li et al. (2015), Lu and Weng (2006), Small (2005), Weng et al. (2009)	Zhang et al. (2016)	Zhang et al. (2014a), Zhu et al. (2012)	Lu et al. (2011a), Lu and Weng (2009), Myint et al. (2011)	
		Unsupervised	Zhang and Seto (2011), Zhou et al. (2014)			Ban et al. (2015)			
		Decision tree	Liu et al. (2012)	Mertes et al. (2015), Schneider et al. (2009, 2010)					
		Object-based	Xie and Weng (2016)					Hu and Weng (2011), Myint et al. (2011), Voltersen et al. (2014)	
Built-up area	Image and spatial statistics-based methods	Supervised			Singh et al. (2012)				
		Object-based						Florczyk et al. (2016), Myint et al. (2011), Pesaresi et al. (2011, 2008, 2013), Pesaresi and Gerhardinger (2011)	Yu et al. (2010)
	Pixel and time series statistics-based methods					This study			

2010 at individual pixels and generate annual built-up maps in the lower Yangtze River Delta, China.

2. Material and methods

2.1. Study area

Our study area is located in the lower Yangtze River Delta of eastern China (Fig. 1) and covers an area of 17,076 km^2. This study area is flat, and the elevation has a range from sea level to 100 m. This region has a marine monsoon subtropical climate, with hot and humid summer, cool and dry winter, and warm spring and fall. The annual mean temperature is 16 °C, with the highest average temperature in July (27.8 °C) and the lowest average temperature in January (3.5 °C). The annual average rainfall is 1160 mm, and 60% is concentrated from May to September.

Cropland and built-up land are the dominant land cover types, and each of them accounts for about 40% of the total land area (Yin et al., 2011). This study area has the largest megacity in China (Shanghai), along with some small to medium cities and rural areas. The built-up land extent has experienced unprecedented expansion since the "reform and opening-up policy" in 1978. The area percentage of built-up land in Shanghai increased from 4% in 1979 to 42% in 2009 (Yin et al., 2011). The total human population increased from 11 million in 1979 to 22 million in 2009, with the population density from 1838 people/km^2 to 3486 people/km^2 (Ma and Ma, 2014).

2.2. Landsat and ALOS PALSAR imagery and preprocessing

We collected time series Landsat TM/ETM+ and ALOS PALSAR images in the study area and carried out image preprocessing (Fig. 2). For Landsat imagery, the preprocessing included atmospheric correction, the identification of bad quality observations (Scan Line Corrector (SLC)-off strips, clouds, cloud shadows, and snow/ice), and calculation of vegetation index, flooding frequency, and annual maximum NDVI ($NDVI_{max}$). For ALOS PALSAR imagery, the preprocessing included converting the digital number (DN) into backscattering coefficient in decibels, median filter, resampling, and calculation of HH and HV gamma-naught.

2.2.1. Landsat TM/ETM+ images and preprocessing

We downloaded all the available Landsat TM and ETM+ images (path/row 118/038) from 2006 to 2011 from the USGS EDC website, a total of 73 Landsat TM images and 101 Landsat ETM+ images. The standard Level 1 Terrain-corrected (L1T) images and other images with different processing levels are all included in the data processing. About 35 images are available in 2006, 2007 and 2008, and about 20 images in 2009, 2010 and 2011, respectively (Fig. 1b).

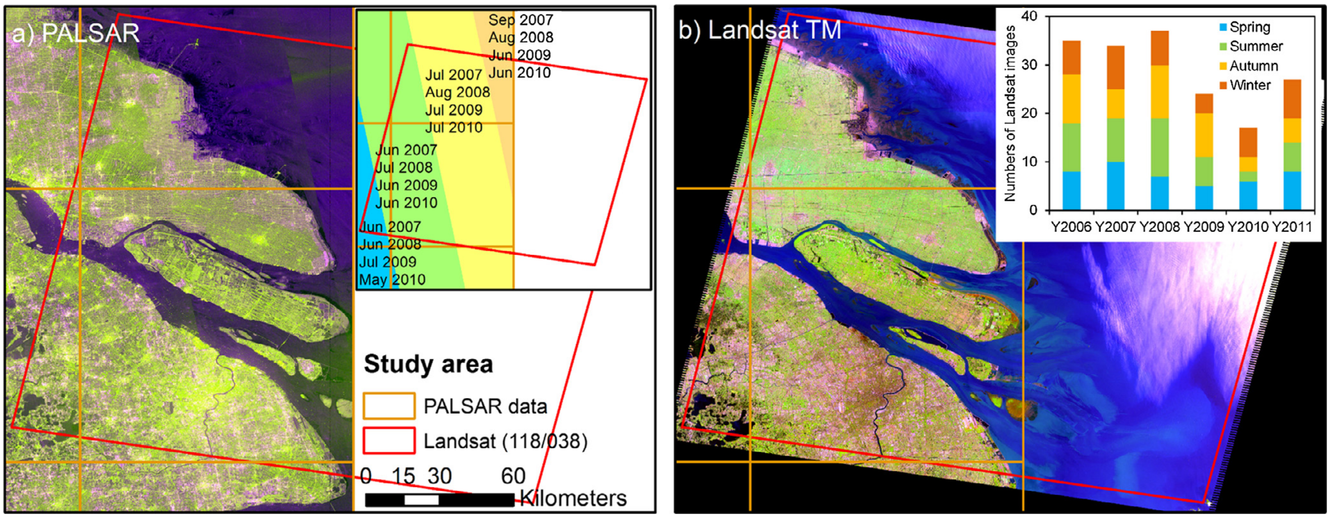

Fig. 1. The location of the study area and data availability in the lower Yangtze River Delta. (a) False color composition of ALOS PALSAR Fine Beam Dual Polarization (FBD) data in 2010: Red (HH), Green (HV) and Blue (HH - HV), and the acquired date of PALSAR FBD data from 2007 to 2010. (b) False color composition of Landsat TM image, acquired on April 18, 2011, with Red (SWIR), Green (NIR) and Blue (Green), and seasonal statistics of the numbers of Landsat TM/ETM+ images from 2006 to 2011. (For interpretation of the references to colour in this figure legend, the reader is referred to the web version of this article.)

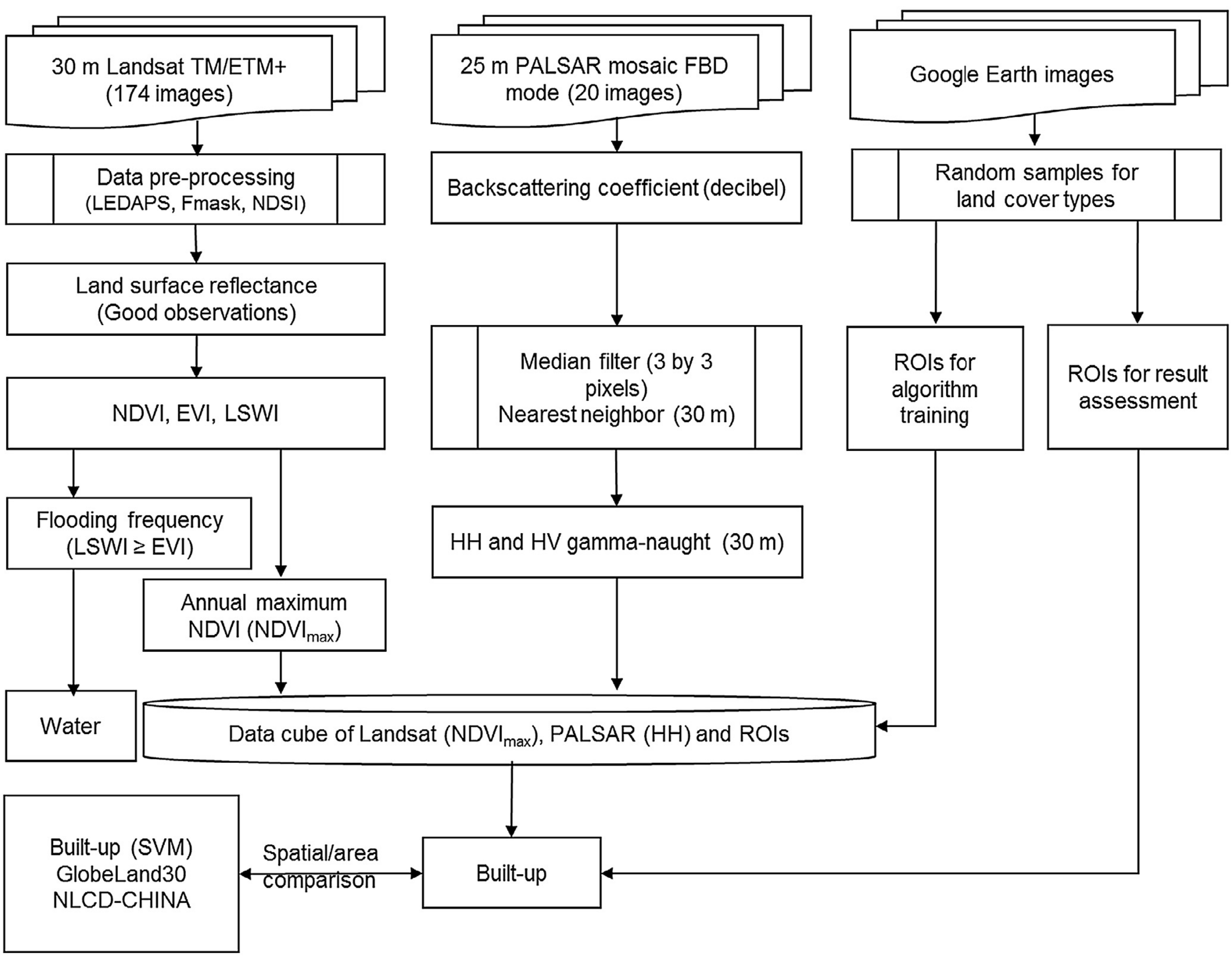

Fig. 2. The workflow for tracking and mapping built-up areas in the lower Yangtze River Delta, based on the combination of Landsat TM/ETM+ and PALSAR FBD images.

2.2.1.1. Atmospheric correction. The Landsat Ecosystem Disturbance Adaptive Processing System (LEDAPS) software was used to convert the raw DN values from Landsat images to land surface reflectance. The LEDAPS applies MODIS 6S radiative transfer models to retrieve top of atmosphere reflectance and land surface reflectance (Masek et al., 2006; Vermote et al., 1997) using Landsat images and ancillary datasets, such as water vapor, ozone, geopotential height, aerosol optical thickness and digital elevation.

2.2.1.2. Bad quality observations. Bad quality observation detection is an essential step for the utilization of optical remote sensing images. In this study, the bad quality observations include SLC-off strips, clouds, cloud shadows, and snow/ice cover. These bad quality observations were excluded for data analysis:

(1) SLC-off strips. The SLC onboard Landsat 7 failed after May 31, 2003, which result in SLC-off strips to Landsat ETM+ images. A SLC-off strips layer (gap_mask) is available to label and mask no observation pixels in individual Landsat ETM+ images.
(2) Clouds and cloud shadows. Clouds and shadows are a significant problem for time series analysis of Landsat imagery (Goodwin et al., 2013), and their detection is an initial step in the most analysis. Fmask software was applied to develop clouds and cloud shadows layers for each of the Landsat TM and ETM+ images (Zhu and Woodcock, 2012).
(3) Snow and ice covers. Snow and ice cover have high reflectance in the visible spectral bands and can potentially affect the values of vegetation indices, especially for Land Surface Water Index (LSWI) and Enhanced Vegetation index (EVI) (Xiao et al., 2006, 2005). We used the Normalized Difference Snow and Ice Index (NDSI) and reflectance of NIR (NDSI > 0.4 and NIR > 0.11) to generate snow/ice masks for each image (Hall et al., 1995, 2002).

2.2.1.3. Statistical analysis of good quality observations of time series Landsat images. The numbers of good quality observations at individual pixels from 1-year Landsat TM/ETM+ images vary over space (Fig. 3a–d). About 98.4%, 98.4%, 98.2% and 97.8% of pixels had more than 10 good quality observations for 2007, 2008, 2009 and 2010, respectively (Fig. 3i). We calculated the percentage of good quality observations at the pixel level, *i.e.*, the ratio of good quality observation numbers to the total observation numbers within a year (Fig. 3e–h). About 89.9%, 94.0%, 95.8% and 96.4% of pixels had more than 20% good quality observations for 2007, 2008, 2009 and 2010, respectively (Fig. 3j).

2.2.1.4. Vegetation indices. We calculated three vegetation indices (NDVI, EVI, and LSWI) for each Landsat image, which were used to analyze the spectral and biophysical features of typical land cover types. NDVI (Rouse et al., 1974) and EVI (Huete et al., 2002, 1997) were used to assess the greenness of land surface. LSWI is sensitive to leaf water and soil moisture (Xiao et al., 2002a,b). We calculated inundation frequency per pixel for each year based on the criteria of LSWI – EVI $\geqslant 0$ (Xiao et al., 2006, 2005). We calculated $NDVI_{max}$ for 2007–2010, respectively (Fig. 4a).

$$NDVI = \frac{\rho_{nir} - \rho_{red}}{\rho_{nir} - \rho_{red}}$$

$$EVI = 2.5 \times \frac{\rho_{nir} - \rho_{red}}{\rho_{nir} + 6 \times \rho_{red} - 7.5 \times \rho_{blue} + 1}$$

$$LSWI = \frac{\rho_{nir} - \rho_{swir}}{\rho_{nir} + \rho_{swir}}$$

where ρ_{blue}, ρ_{red}, ρ_{nir} and ρ_{swir} are the land surface reflectance values of Blue (0.45–0.52 μm), Red (0.63–0.69 μm), NIR (0.77–0.90 μm) and SWIR (1.55–1.75 μm) band for Landsat TM/ETM+ images.

2.2.2. 25-m ALOS PALSAR ortho-rectified mosaic dataset and preprocessing

The 25-m PALSAR ortho-rectified mosaic data at Fine Beam Dual Polarization (FBD) mode from 2007 to 2010 is available from Japan Aerospace Exploration Agency (JAXA). They were aggregated from the original observation with minimum response to surface moisture (Shimada et al., 2014). The dataset is organized in latitude-longitude coordinates and has 4500 columns by 4500 rows per tile. The dataset includes HH and HV gamma-naught backscatter, local incidence angle and mask information, and total dates since the ALOS launch. The local incidence angle ranges from 36° to 40°. The HH and HV data are slope corrected and orthorectified, radiometrically calibrated, and normalized by the realistic illumination area.

The PALSAR HH and HV DN values (amplitude values) were converted into gamma-naught in decibel using a calibration coefficient $\gamma^{\circ} = 10 \times \log_{10}\langle DN^2 \rangle - 83$, which is insensitive to the focus of the impulse response (Shimada et al., 2009). A 3 by 3 pixel median filter was applied on PALSAR HH and HV imagery to reduce speckle noise. We resampled the 25-m PALSAR HH and HV imagery into 30-m imagery (Fig. 4c and d) to match 30-m Landsat imagery using the nearest neighborhood interpolation.

2.3. Ground reference data for approach training and validation from very high spatial resolution images

As the landscape is complex and fragmented, relatively small sizes of Region of Interests (ROIs) are needed in order to reduce the effect of mixed pixels on ROIs. We generated randomly 2000 60-m × 60-m (2 by 2 pixels at 30-m spatial resolution) rectangles (ROIs) in the shapefile format, with a minimum distance of 1000 m between ROIs. These 2000 polygons were converted into kml format and overlaid to very high spatial resolution images in Google Earth. The very high spatial resolution images of the main growing season for each year were selected for land cover type interpretation. If no image was available in a certain year, the very high spatial resolution images before and after this year were all chosen as the referenced images. A pixel within a 60-m × 60-m rectangle was classified as a ROI for built-up area if it has 50% or more area occupied by building structure. A pixel within a 60-m × 60-m rectangle, if occupied by 50% or more non building structure area, was classified as a non built-up ROI. We then overlaid these annual training samples spatially and determined the common ROIs over the four years. In total, 980 pixel ROIs are common (consistent) from 2007 to 2010, and thus used for approach training (Table 2). These include 320 built-up pixel ROIs, 104 forest pixel ROIs, 172 cropland pixel ROIs, 80 pond pixel ROIs, and 304 wetland pixel ROIs, respectively. The spatial distribution of selected ROIs for approach training is shown in Fig. 5a.

We also generated randomly 3000 60-m × 60-m rectangles to select ROIs for accuracy assessment of the annual built-up/non built-up maps. In total, the built-up ROIs have 276 pixels, 308 pixels, 384 pixels, and 416 pixels, and the non built-up ROIs have 2278 pixels, 2326 pixels, 3308 pixels, and 3892 pixels in 2007, 2008, 2009 and 2010, respectively (Table 2). Then we used these ROIs to build a confusion matrix for accuracy assessment of built-up/non built-up map in each year, including overall accuracy, kappa coefficient, producer accuracy/omission error, and user accuracy/commission error.

2.4. Approaches for identifying built-up area through PALSAR and Landsat images

Compared with other land cover types, built-up area has three of the following biophysical features. First, built-up area is covered by various human-made materials with different colors, shapes, and spectral characteristics. Second, built-up area is usually mixed with other land cover types (e.g., trees, shrubs, grassland, and water bodies), and have low greenness. Third, built-up area has an obvious 3-dimensional structure above the ground.

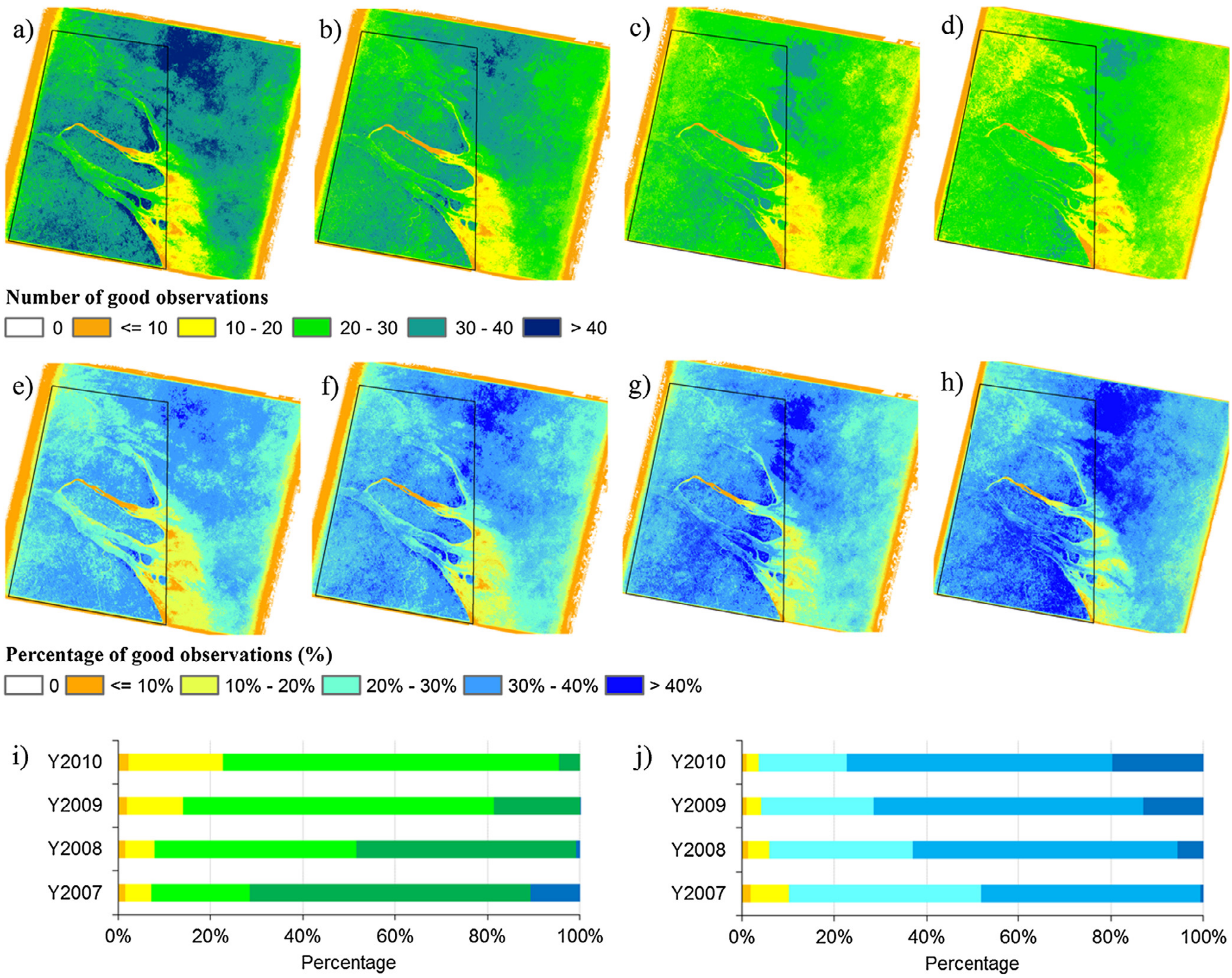

Fig. 3. The numbers and percentage of good quality observations at pixel level from 1-year Landsat TM/ETM+ images. (a–d) and (e–h) are the numbers and percentage of good quality observations of Landsat images in nominal years (3-year moving window), Y2007 (2006–2008), Y2008 (2007–2009), Y2009 (2008–2010), and Y2010 (2009–2011), respectively. (i) and (j) are the statistics of the numbers and percentage of Landsat good quality observations for 2007, 2008, 2009, and 2010, respectively.

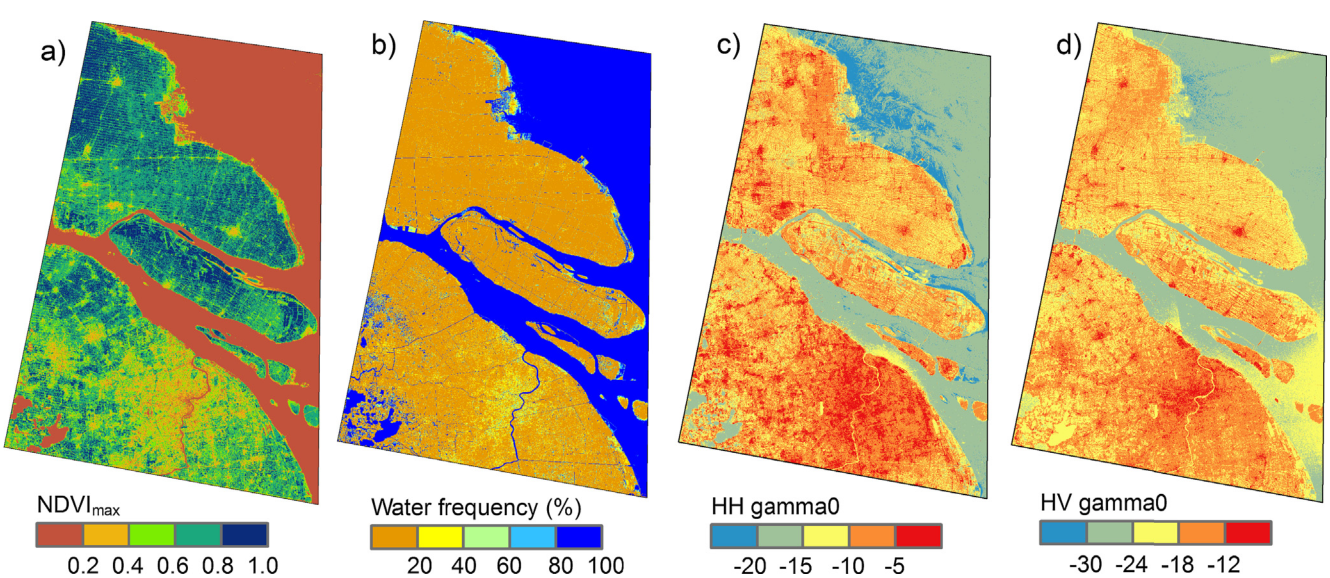

Fig. 4. The spatial distribution of annual maximum NDVI (a), water frequency (b), HH gamma-naught (c), and HV gamma-naught (d) in 2010.

Table 2
Annual ground reference data (ROIs#) for the approach training of built-up area identification and the validation of the resultant built-up/non built-up maps from 2007 to 2010.

Land cover		2007	2008	2009	2010
Training samples	Built-up	320	320	320	320
	Forest	104	104	104	104
	Cropland	172	172	172	172
	Pond	80	80	80	80
	Wetland	304	304	304	304
	Total	980	980	980	980
Validation samples	Built-up	276	308	384	416
	Non Built-up	2278	2326	3308	3892
	Total	2554	2634	3692	4208

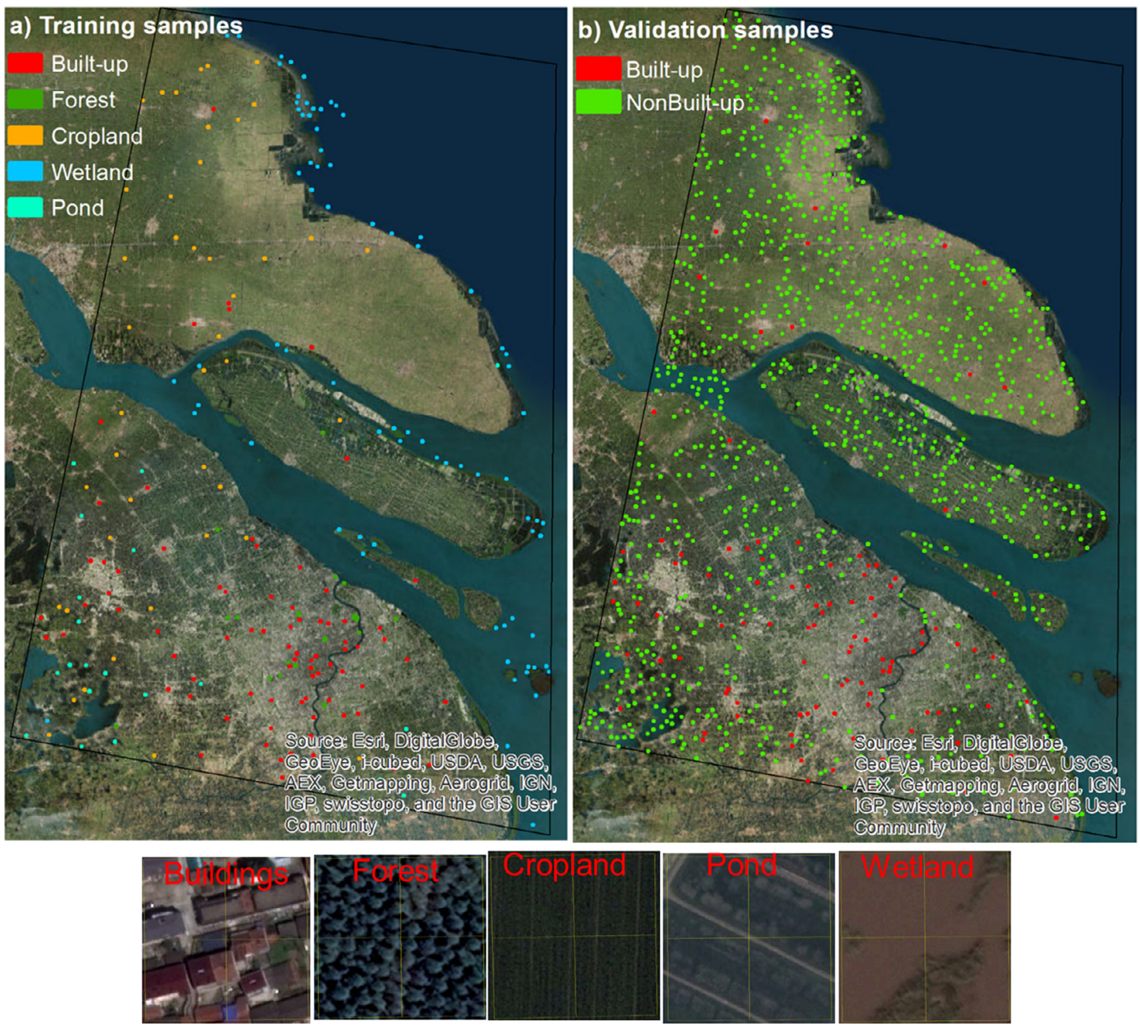

Fig. 5. Random ground reference for approach training (a) and map accuracy assessment (b) of built-up area at the spatial resolution of 60 m in 2010, acquired from very high spatial resolution images in Google Earth.

2.4.1. Signature analysis of land cover types with Landsat and PALSAR images

Fig. 6 shows an example of the 2-dimensional scatter plot/density maps of PALSAR HH and Landsat $NDVI_{max}$, and PALSAR HV and Landsat $NDVI_{max}$ in the Yangtze River Delta in 2010. Most of the water pixels have low HH, HV, and $NDVI_{max}$ values. The other land cover types hold their specific distribution patterns, while their HH, HV, and $NDVI_{max}$ boundaries are blurred, which may be contributed to by the mixed pixels in the fragmented landscapes.

For signature analysis of major land cover types, we investigated the relationship between $NDVI_{max}$ and HH, and HV for each year. We calculated their mean and standard deviation values and generated eight 2-dimensional scatter plots between $NDVI_{max}$ and HH, and HV of typical land cover types from 2007 to 2010, respectively (Fig. 7). Built-up and forests show high backscatter values in both HH and HV due to their strong corner reflectance. Forests have leaves, branches, stems and trunks, which can result in relatively more complex structure and internal reflection environment than those of built-up areas. Therefore, built-up areas have relatively stronger backscatter in HH, and weaker backscatter in HV than those of forests. Croplands, wetlands, and ponds have low backscatter values in both HH and HV. Therefore, HH is selected for mapping built-up area in this study.

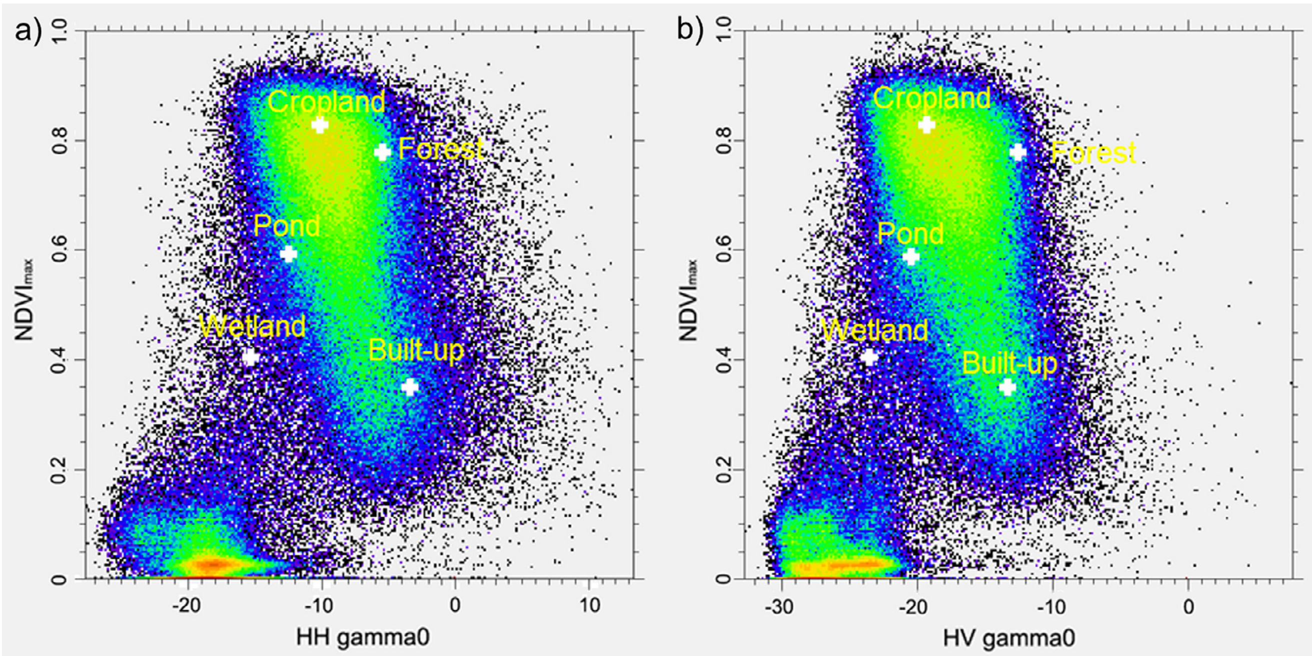

Fig. 6. 2-dimension scatter plots of (a) HH gamma-naught and $NDVI_{max}$, and (b) HV gamma-naught and $NDVI_{max}$ in the study area in 2010. The white crosses are the mean values of HH gamma-naught, HV gamma-naught, and $NDVI_{max}$ for typical land cover types.

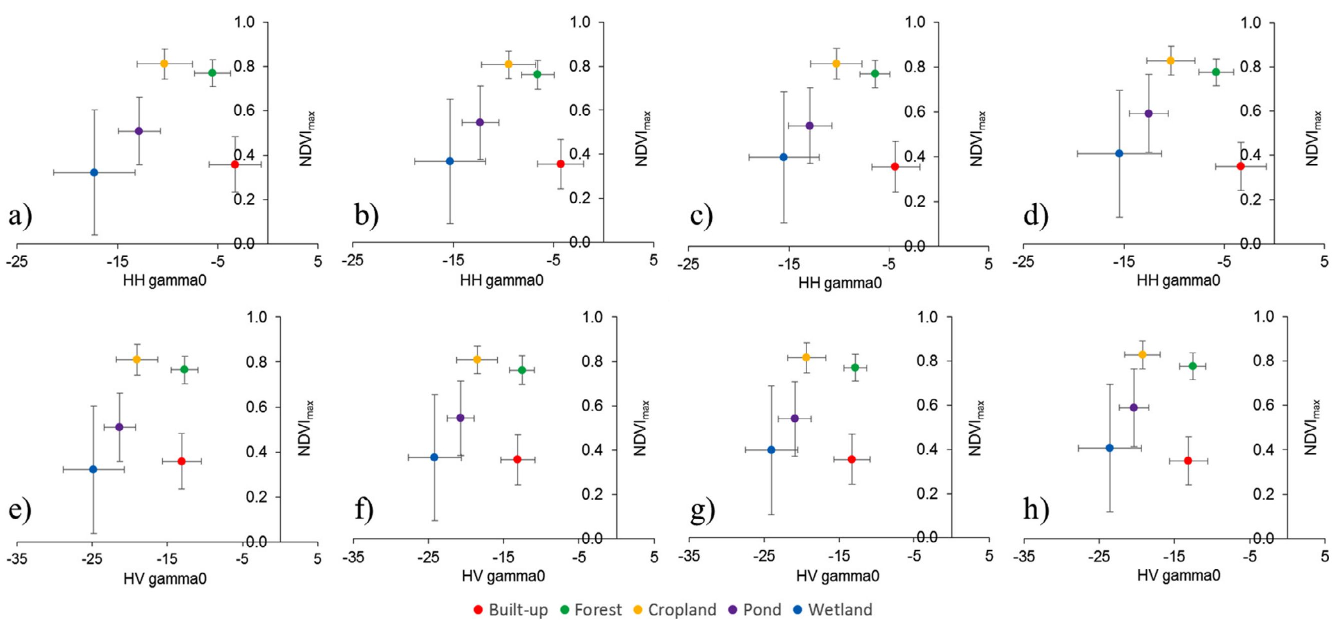

Fig. 7. The mean value and standard deviation of typical land cover types from Landsat and PALSAR images. (a–d) are 2-dimension scatter plots between HH gamma-naught and annual maximum NDVI ($NDVI_{max}$) from 2007 to 2010, respectively. (e–h) are 2-dimension scatter plots between HV gamma-naught and $NDVI_{max}$ from 2007 to 2010, respectively.

$NDVI_{max}$ shows good ability to distinguish built-up area from other typical land cover types (Fig. 7). Built-up have a relatively low amount of vegetation, and their average $NDVI_{max}$ values are around 0.4, while forests and croplands have large vegetation and their average $NDVI_{max}$ values are around 0.8. Thus, $NDVI_{max}$ is used to further reduce commission errors from forests and croplands, and refine built-up area.

2.4.2. Approaches to identify built-up area

We first excluded the boats and wetlands in the Yangtze River, as they may have similar backscatter features with built-up area. We generated an open surface water body map using time series Landsat images in each year. The algorithm counted the numbers of observations in which a pixel had LSWI – EVI $\geqslant 0$ out of all the good quality observations and then divided it by the total number of good quality observations (Dong et al., 2015; Xiao et al., 2006, 2005). Those pixels with a resultant ratio value $\geqslant 80\%$ are identified as year-long open surface water body (Fig. 4b).

PALSAR HH and Landsat $NDVI_{max}$, representing the structure and greenness, showed stable features for built-up area during 2007–2010 (Fig. 7a–d) and were selected to map built-up area.

Table 3
Summary of built-up area and impervious surface maps generated by multiple data sources and approaches in 2010.

Products	Definition	Data source	Training data	Approach	Minimum unit (m^2)	Validation data	Spatial resolution (m)	Accuracy
PALSAR/Landsat	Land covered by 50% or more building structure	PALSAR HH and Landsat $NDVI_{max}$	320 and 660 random selected ROIs for built-up and non built-up, respectively	Decision tree	900	416 and 3892 random selected ROIs for built-up and non built-up, respectively	30	UA: 87%, PA: 94%
PALSAR/Landsat$_{SVM}$	Same as above	Same as above	Same as above	SVM	900	Same as above	30	UA: 72%, PA: 97%
Globeland30 (Chen et al., 2015)	Artificial surfaces (urban areas, roads, rural cottages and mines)	Single Landsat TM/ETM+ and HJ-1 with few clouds	NA	A pixel-object-knowledge-based (POK-based) classification approach	14,400	159,874 pixel samples were selected from 80 map sheet samples	30	UA: 87%
NLCD-CHINA (Liu et al., 2014)	Urban, rural settlement and industry-traffic land	Single Landsat TM (90%), CBERS, and HJ-1A	Interpretation symbols for each land use/cover type	Visual interpretation	40,000	Repeated interpretation of randomly extracted 10% counties. Extensive field survey	1000 (fraction)	OA: 95%

UA: User accuracy, PA: Producer accuracy, and OA: Overall accuracy.

Built-up areas are featured in high HH backscatter values and low $NDVI_{max}$ values (~0.6). Built-up are likely to be confused with parts of forest in HH, but forest has large leaf area index (LAI), often higher than 3 m^2/m^2 (Gamon et al., 1995; Turner et al., 1999), which corresponds to $NDVI_{max}$ values larger than 0.7 (Gamon et al., 1995; Jiao et al., 2014; Turner et al., 1999). To reduce the confusion error, the lowest 5% of HH gamma-naught and the highest 5% $NDVI_{max}$ values of ground reference for built-up were excluded at the 95% confidence level. The uniform values of HH and $NDVI_{max}$ at the 95% confidence level, calculated based on the training datasets, were chosen as the thresholds to map built-up area from 2007 to 2010:

$$(HH \geqslant -9)\ \&\&\ (NDVI_{max} < 0.6)$$

A temporal and logical consistency check was applied to reduce the commission and omission errors of built-up areas (Schneider and Mertes, 2014). Each pixel from 2007 to 2010 has 16 different built-up (B) and non built-up (N) permutation over years. The reasonable (NNNN, NNNB, NNBB, NBBB, BNNN, BBNN, BBBN and BBBB) and irregular (NBNB, NBBN, BNNB and BNBN) permutation remained to be unchanged, while the consistency filter was applied to the unreasonable permutation (NNBN → NNNN, NBNN → NNNN, BNBB → BBBB, and BBNB → BBBB). After this consistency check, we generated annual maps of built-up areas (PALSAR/Landsat) in 2007–2010.

2.5. Comparison between the built-up maps and impervious surface maps generated by multiple data sources and approaches

In this study, another four annual built-up maps (PALSAR/Landsat$_{SVM}$) were generated by the image-based SVM approach and the same input datasets, *i.e.*, PALSAR HH and Landsat $NDVI_{max}$, as did our pixel- and rule-based approach. We also collected two other impervious surface products to compare their consistency and differences, including 30-m Globeland30 (Chen et al., 2015) and 1-km fraction NLCD-China (Liu et al., 2014). Table 3 shows the general information about the built-up areas and impervious surface maps. We analyzed the consistency and difference between the built-up areas and the impervious surface maps.

The Globeland30 impervious surface map in 2010: The Globeland30 dataset uses a 10 first-level classification scheme, including artificial surfaces (Chen et al., 2015). Landsat TM/ETM+ images with minimal cloud contamination and the Chinese Environmental and Disaster satellite (HJ-1) images were used to produce Globeland30 through a proposed pixel-object-knowledge (POK-based) classification approach. Each land cover type is determined in a prioritized sequence and then the results are merged together. A knowledge-based interactive verification is then carried out to check and improve the classification results. The overall accuracy of Globeland30 is about 80% and the user's accuracy of artificial surfaces is about 87%.

The NLCD-China impervious surface map in 2010: NLCD-China datasets were generated almost every five years from the late 1980s to 2010, and the impervious surface is one of six land cover types (Kuang et al., 2016; Liu et al., 2014). 30-m Landsat TM/ETM+, the China-Brazil Earth Resources Satellite (CBERS), and HJ-1A images with minimum cloud coverage in the vegetation growing season were selected to generate NLCD-China. Geometric correction was done for all the satellite images using ground control points, with the relative position error less than two pixels. Four steps were implemented in the NLCD-China classification projects (Zhang et al., 2014b). First, interpretation symbols were built for the typical land use/cover types, according to the field survey. Second, the baseline NLCD-China for 1995 was produced. Interpreters analyzed and identified land use/cover types from Landsat TM images in 1994/1995, then digitalized the boundaries and labeled the properties for each polygon at the scale of 1:100,000. Third, interpreters compared the satellite images during different periods and digitalized the land use and land cover changes (LULCC). Fourth, the NLCD-China in 1995 and the LULCC polygons from 1995–2010 were combined together to produce the NLCD-China in 2010. The vector data was intersected with a 1 km × 1 km fishnet, and the area percentages of individual land cover types were calculated as the values for each gridcell. NLCD-China was validated with a high accuracy of about 95% for the 6 classes, using the re-interpretation map of randomly 10% of counties and field survey photos (Zhang et al., 2014b).

3. Results

3.1. Spatial distribution and area estimation of built-up land from the 30-m PALSAR/Landsat and PALSAR/Landsat$_{SVM}$ built-up maps in the Yangtze River Delta

Fig. 8 shows the annual PALSAR/Landsat and PALSAR/Landsat$_{SVM}$ built-up areas at the spatial resolution of 30 m in the Yangtze River Delta from 2007 to 2010. They have similar spatial distribution patterns in annual maps of built-up areas. The southern region is dominated by the megacity of Shanghai, with large areas of urban and peri-urban built-up areas. The northern region is part of Yangtze Plain, a major agriculture production region in China, and the rural built-up areas are widely distributed in a linear pattern. The areas of the built-up land from the PALSAR/Landsat built-up map were about 2565 km^2 (15.02% of the total study area), 2591 km^2 (15.17%), 2599 km^2 (15.22%) and 2805 km^2 (16.42%) from 2007 to 2010, while the area of the built-up land from the PALSAR/Landsat$_{SVM}$ built-up map were relatively higher, about 3145 km^2 (18.42%), 3254 km^2 (19.06%), 3343 km^2 (19.58%), and 3152 km^2 (18.46%), respectively.

3.2. Accuracy assessment of built-up maps in the Yangtze River Delta

We calculated the confusion matrix based on the built-up and non built-up ROIs (Section 2.3) and used them to assess the accuracy of the built-up maps (Table 4). Both PALSAR/Landsat and PALSAR/Landsat$_{SVM}$ built-up maps were assessed with high accuracies. Each PALSAR/Landsat built-up map has an overall accuracy around 98%, and Kappa coefficient close to 0.90 or above from 2007 to 2010. Non built-up category has relatively higher user and producer accuracies than those of built-up category. The user accuracies of built-up areas are 86.9%, 92.7%, 89.9% and 88.2% from 2007 to 2010, which is slightly lower than their producer accuracies (91.3%, 95.1%, 92.2% and 93.5%). Compared with PALSAR/Landsat built-up maps, PALSAR/Landsat$_{SVM}$ built-up maps have slightly lower overall accuracy (about 96%) and relatively higher commis-

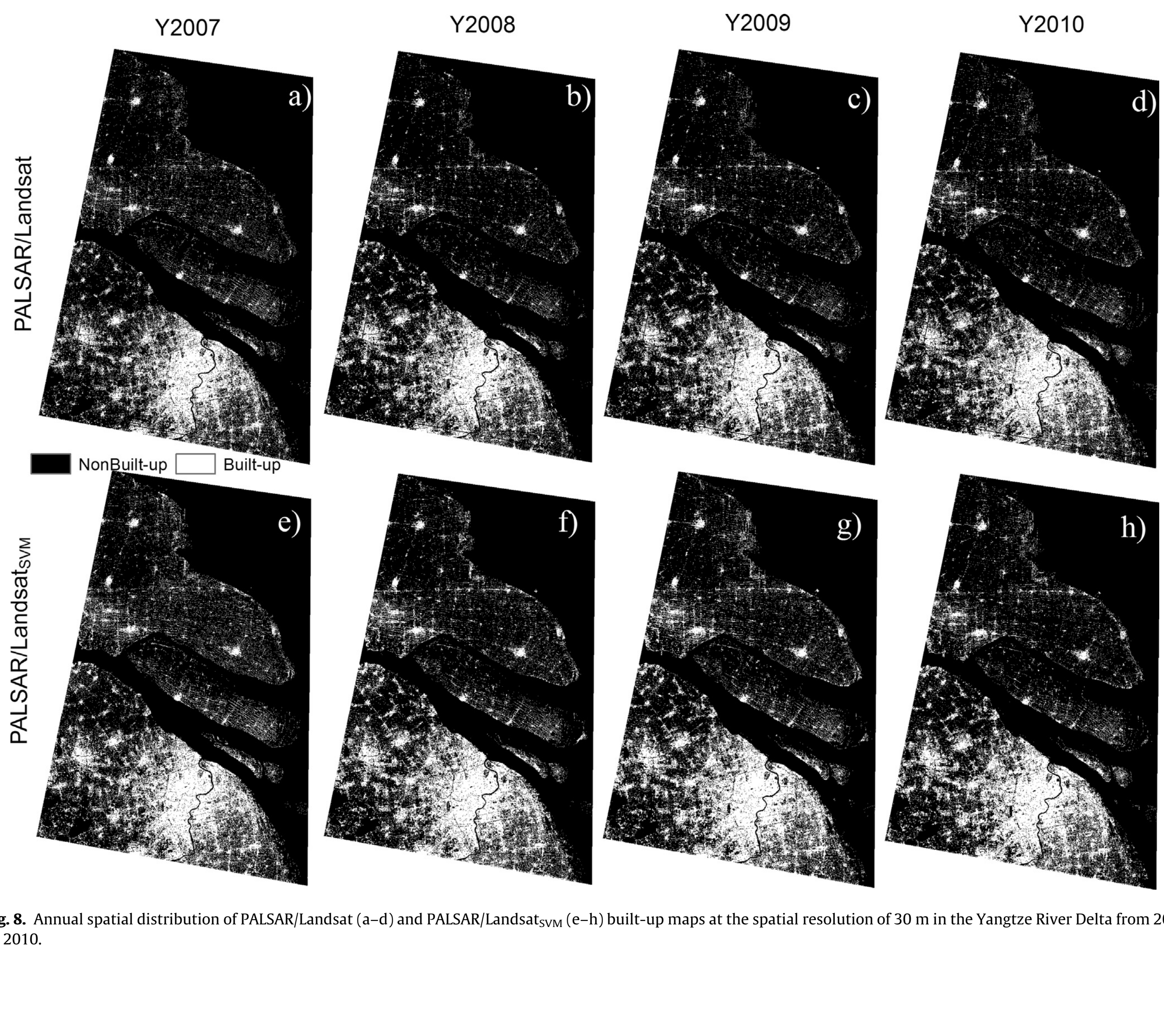

Fig. 8. Annual spatial distribution of PALSAR/Landsat (a–d) and PALSAR/Landsat$_{SVM}$ (e–h) built-up maps at the spatial resolution of 30 m in the Yangtze River Delta from 2007 to 2010.

Table 4
Accuracy assessment of annual built-up maps in the Yangtze River Delta, using the ground reference data selected from very high spatial resolution images in Google Earth.

Year	Land cover	PALSAR/Landsat built-up			PALSAR/Landsat$_{SVM}$ built-up		
		User accuracy/ Commission error (%)	Producer accuracy/ Omission error (%)	Overall accuracy (%)/ Kappa coefficient	User accuracy/ Commission error (%)	Producer accuracy/ Omission error (%)	Overall accuracy (%)/ Kappa coefficient
2007	Built-up	86.90/13.10	91.30/8.70	97.57/0.88	78.79/21.21	94.20/5.80	96.63/0.84
	Non built-up	98.94/1.06	98.33/1.67		99.28/0.72	96.93/3.07	
2008	Built-up	92.72/7.28	95.13/4.87	98.56/0.93	79.00/21.00	97.73/2.27	96.70/0.86
	Non built-up	99.35/0.65	99.01/0.99		99.69/0.31	96.56/3.44	
2009	Built-up	89.85/10.15	92.19/7.81	98.10/0.90	73.12/26.88	96.35/3.65	95.94/0.81
	Non built-up	99.09/0.91	98.79/1.21		99.56/0.44	95.89/4.11	
2010	Built-up	88.21/11.79	93.51/6.49	98.17/0.90	79.13/20.87	96.63/3.37	97.21/0.85
	Non built-up	99.30/0.70	98.66/1.34		99.63/0.37	97.28/2.72	

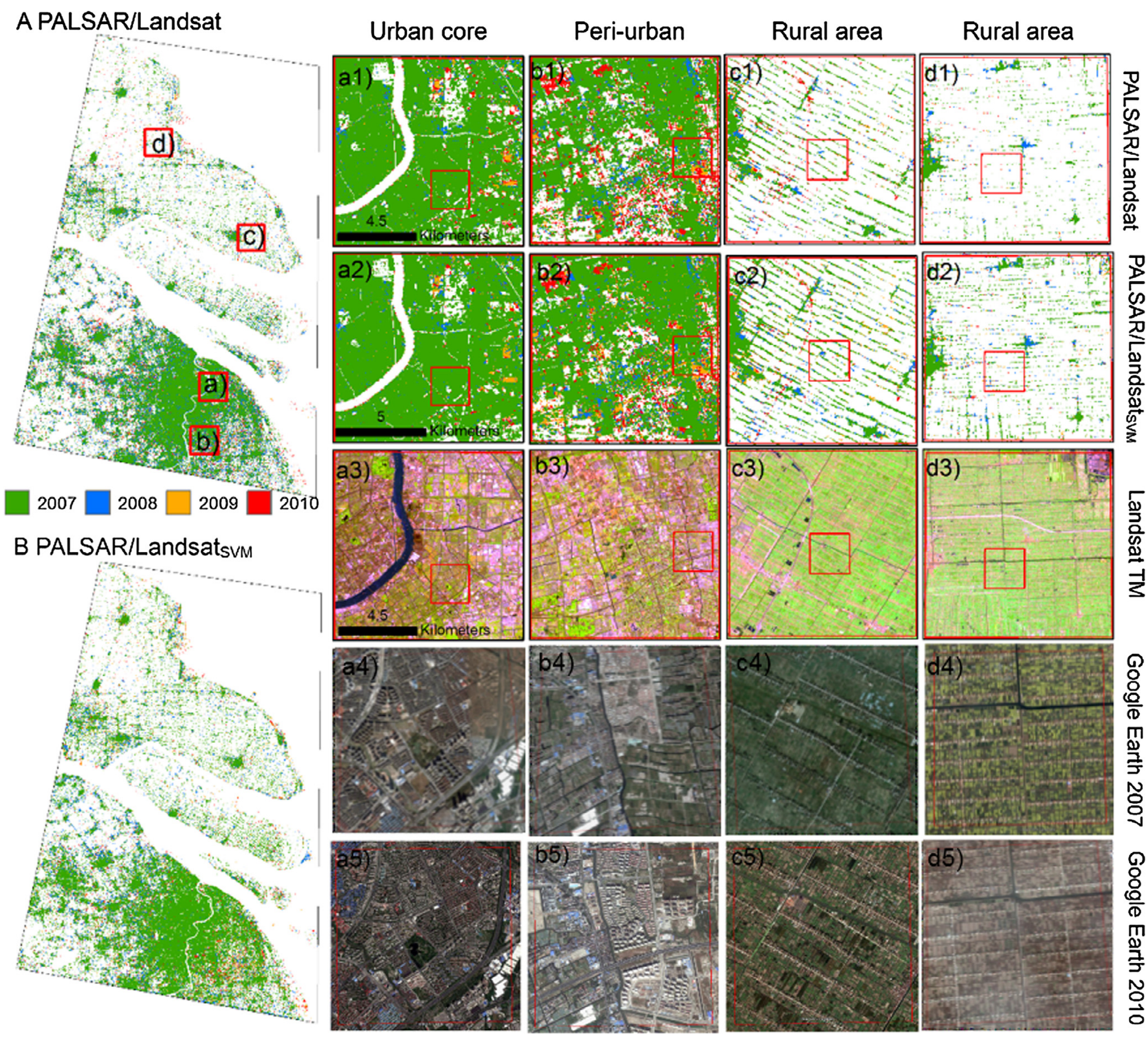

Fig. 9. Spatio-temporal changes of 30-m PALSAR/Landsat (A) and PALSAR/Landsat$_{SVM}$ (B) built-up areas from 2007 to 2010. (a) Built-up in the urban core area, (b) built-up in peri-urban area, (c) and (d) built-up in rural area. (a1–d1) are the zoom-in PALSAR/Landsat built-up areas. (a2–d2) are the zoom-in PALSAR/Landsat$_{SVM}$ built-up areas. (a3–d3) are Landsat TM image acquired on April 18, 2011, with the false color composition: R (SWIR), G (NIR), and B (Green). (a4–d4) and (a5–d5) are high spatial resolution images from Google Earth acquired around 2007 and 2010, respectively.

sion errors for built-up category (about 21%). The moderate commission errors may come from the mixed pixels in the complex and fragmented landscapes.

3.3. Built-up expansion in the Yangtze River Delta from 2007 to 2010

We used the annual PALSAR/Landsat and PALSAR/Landsat$_{SVM}$ built-up maps to identify their spatio-temporal changes during 2007–2010, respectively (Fig. 9). According to the PALSAR/Landsat built-up maps, built-up area continued to increase under the influence of economic development and increasing population, with an average increase of 80 km^2 per year. Built-up areas showed obvious spatio-temporal change patterns. Firstly, the extent of most built-up area is stable, especially in the urban core areas (Fig. 9a), which usually has the priority to be developed with a high density of built-up. Secondly, the spatial changes of built-up areas were characterized by outward expansion (urban sprawl), mainly located in the peri-urban areas (Fig. 9b). Thirdly, some of rural built-up were out of detection because of the low coverage of built-up in mixed pixels (Fig. 9c and d). The PALSAR/Landsat$_{SVM}$ showed similar spatio-temporal change patterns of built-up area in the Yangtze River Delta.

4. Discussion

4.1. A comparison of built-up area identification approaches: image-based SVM versus pixel- and rule-based decision tree

Both the pixel- and rule-based approach and the image-based SVM approach were employed to identify and map annual built-up area from 2007 to 2010 in the Yangtze River Delta. The pixel- and rule-based decision tree approach has relatively simple, explicit and intuitive classification structure, and no assumption about the distribution of input dataset (Friedl and Brodley, 1997). Built-up areas have similar spectral, spatial and texture features (Weng, 2012). The thresholds for built-up identification in PALSAR HH and Landsat NDVI$_{max}$ are consistent from 2007 to 2010, based on their feature analysis from the ground reference data (Fig. 7). Image-based SVM is derived from statistical learning theory and separates land classes with a decision surface that maximized the margin between classes. SVM has three major disadvantages (Suykens et al., 2003): (1) high algorithmic complexity, (2) extensive memory requirements, and (3) certain risk that some pixels may not fit the user-defined classes.

The training/validation strategy and remote sensing input datasets could affect the efficiency and accuracy for identifying and mapping built-up areas. Urban and rural landscapes are fragmented and complex in the Yangtze River Delta. Very high resolution images, such as IKONOS and QuickBird, were used as the reference to select random training and validation samples. Some of these very high resolution images acquired in different time have position offset over one Landsat pixel caused by imperfect geometric calibration and orthorectification, which would cause some uncertainty to the training and validation samples. Due to the heterogeneity of landscapes and 30-m spatial resolution of Landsat and PALSAR images, mixed pixels with less than 50% built-up area are common in urban landscapes, which has been recognized as a major problem for the pixel- and rule-based approach to estimate built-up areas (Weng, 2012). Compared with the pixel- and rule-based approach, the SVM-based approach captures relatively more built-up area in the rural and peri-urban area with low-density built-up but has much larger commission error (Table 4 and Figs. 10 and 11).

PALSAR/Landsat built-up maps had good agreement with PALSAR/Landsat$_{SVM}$ built-up maps from 2007 to 2010. Fig. 10 showed the spatial comparison between PALSAR/Landsat built-up maps and PALSAR/Landsat$_{SVM}$ built-up maps. The urban core areas have a high density of built-up and not much vegetation coverage, and both pixel-based decision tree and image-based SVM work well for built-up identification and present good consistency. In total, about 96.5%, 95.9%, 95.3% and 97.1% of built-up and non built-up were identified by both the pixel- and rule-based approach and the image-based SVM for 2007, 2008, 2009 and 2010, respectively (Fig. 10). The SVM overestimated the built-up area by about 585 km^2 (3.4% of the total area), 680 km^2 (4.0%), 770 km^2 (4.5%) and 418 km^2 (2.4%), in comparison to the pixel- and rule-based

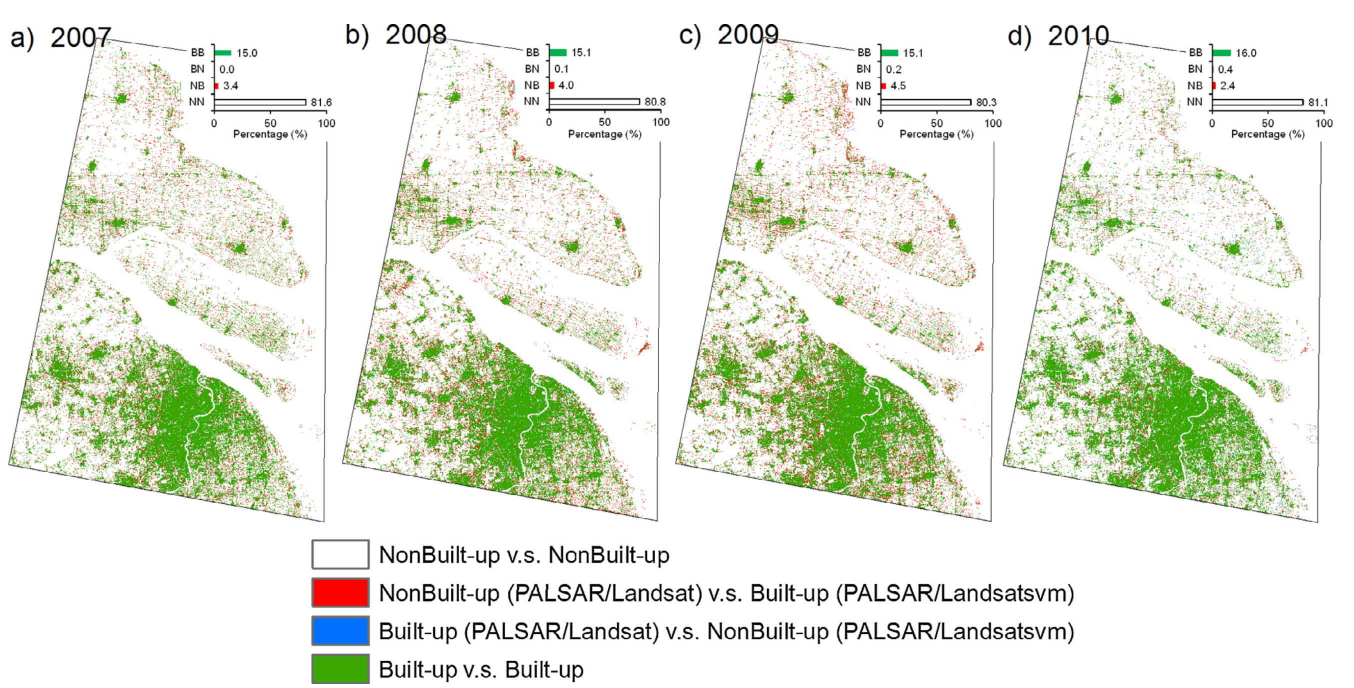

Fig. 10. Spatial comparison between PALSAR/Landsat built-up maps and PALSAR/Landsat$_{SVM}$ built-up maps from 2007 to 2010.

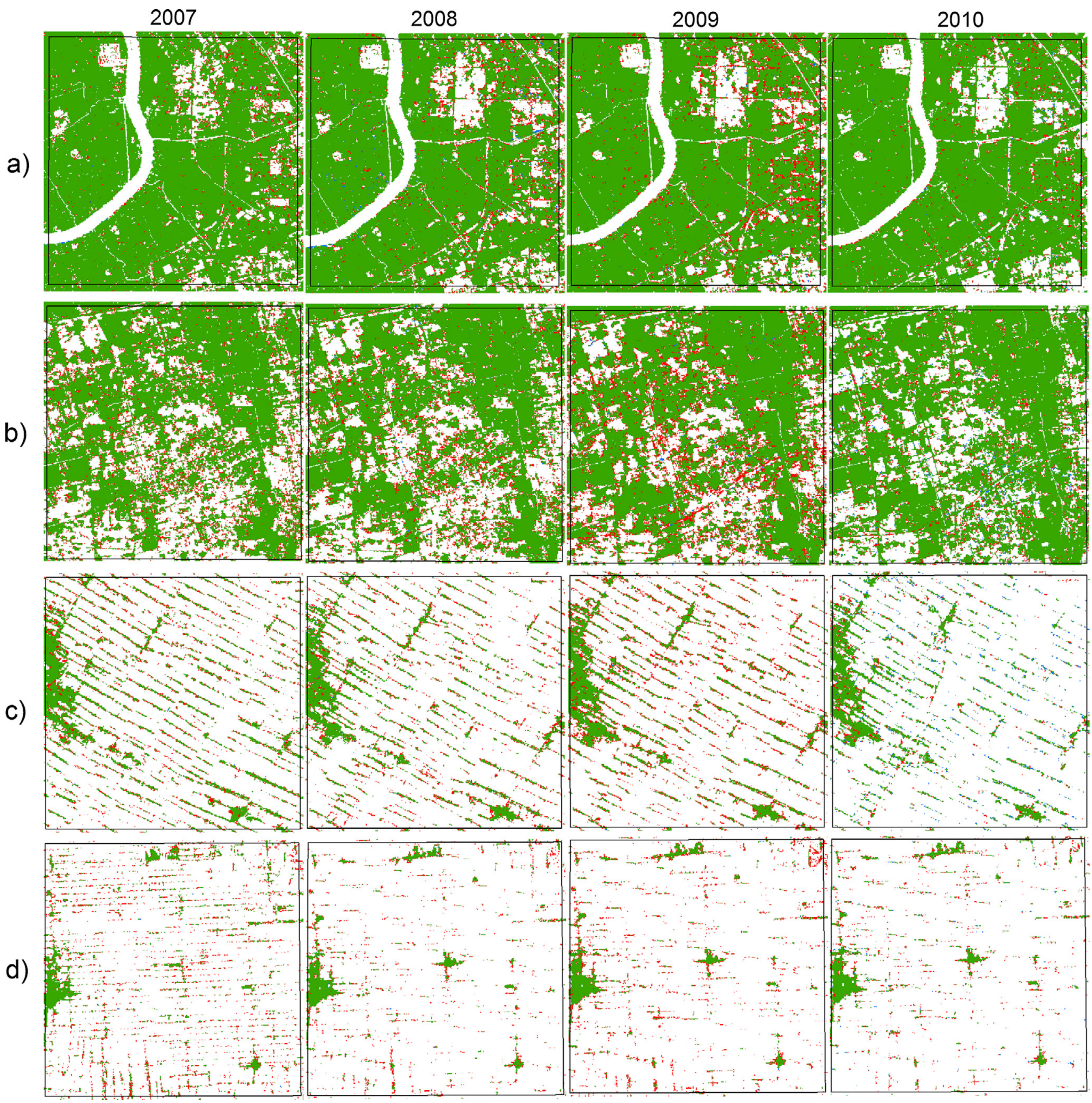

Fig. 11. Zoom-in regions of the spatial comparison between PALSAR/Landsat built-up and PALSAR/Landsat$_{SVM}$ built-up from 2007 to 2010.

decision tree approach for 2007, 2008, 2009 and 2010, respectively. These overestimated pixels were mainly located at the edge of urban areas, or in peri-urban and rural areas (Fig. 11), contributed to by the mixed pixels of built-up and other land cover types. In addition, PALSAR/Landsat and PALSAR/LandsatSVM built-up areas changed from $2383 \pm 60\ km^2$ to $2573 \pm 47\ km^2$ and from $2578 \pm 75\ km^2$ to $2546 \pm 59\ km^2$ from 2007 to 2010 after area adjustment (Olofsson et al., 2014), and the built-up maps identified by SVM does not show the continuity of built-up expansion.

4.2. A comparison between the maps of built-up area and the maps of impervious surfaces

Built-up, with an obvious 3-dimensional structure above the ground, is a subset of impervious surfaces and has a smaller area and spatial extent than those of impervious surfaces. We aggregated these built-up and impervious surface maps from original spatial resolutions into 1-km fraction maps using nearest neighborhood resampling algorithm. Fig. 12 showed the spatial distributions of the built-up maps from PALSAR/Landsat and PALSAR/Landdsat$_{SVM}$, and the impervious surface maps from GlobeLand30 and NLCD-China at the spatial resolution of 1-km in 2010. Generally, all these four built-up and impervious surface maps showed a similar spatial pattern. Both the GlobeLand30 and NLCD-China were generated by interactive visual interpretation of single Landsat TM/ETM+ images, therefore, they had a reasonable estimation of impervious surface area, except for the rural area and peri-urban area with low-density built-up and impervious surface areas (Chen et al., 2015; Liu et al., 2014). The impervious surface areas estimated by the GlobeLand30 ($3151\ km^2$) and NLCD-China

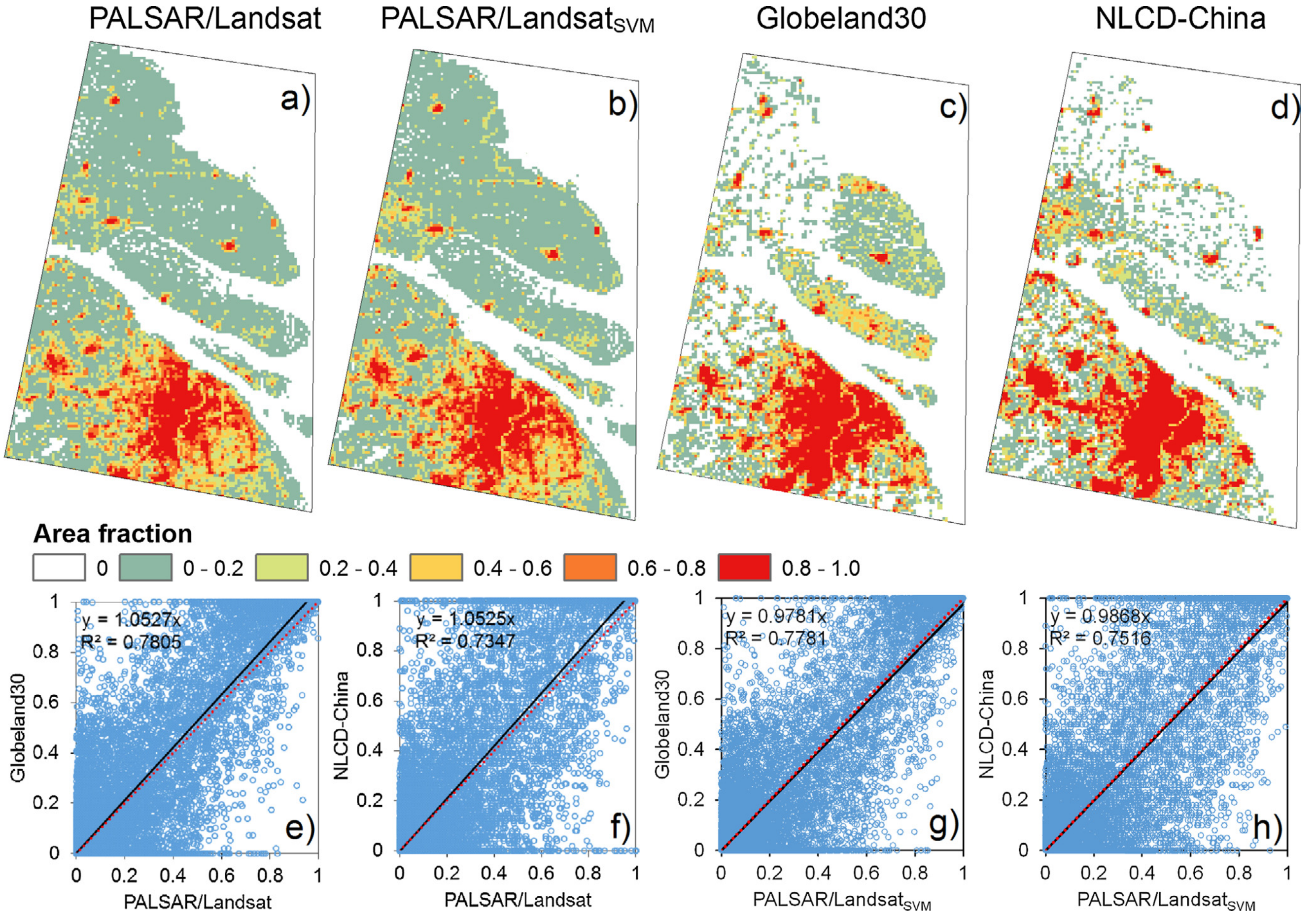

Fig. 12. Spatial distribution of built-up and impervious surface maps at the spatial resolution of 1-km in 2010. (a) PALSAR/Landsat built-up map, (b) PALSAR/Landsat$_{SVM}$ built-up map, (c) Globeland30 impervious surface map, and (d) NLCD-China impervious surface map. Linear relationships between PALSAR/Landsat built-up map and Globeland30 (e) and NLCD-China (f) impervious surface maps, and between PALSAR/Landsat$_{SVM}$ built-up map and Globeland30 (g) and NLCD-China (h) impervious surface maps.

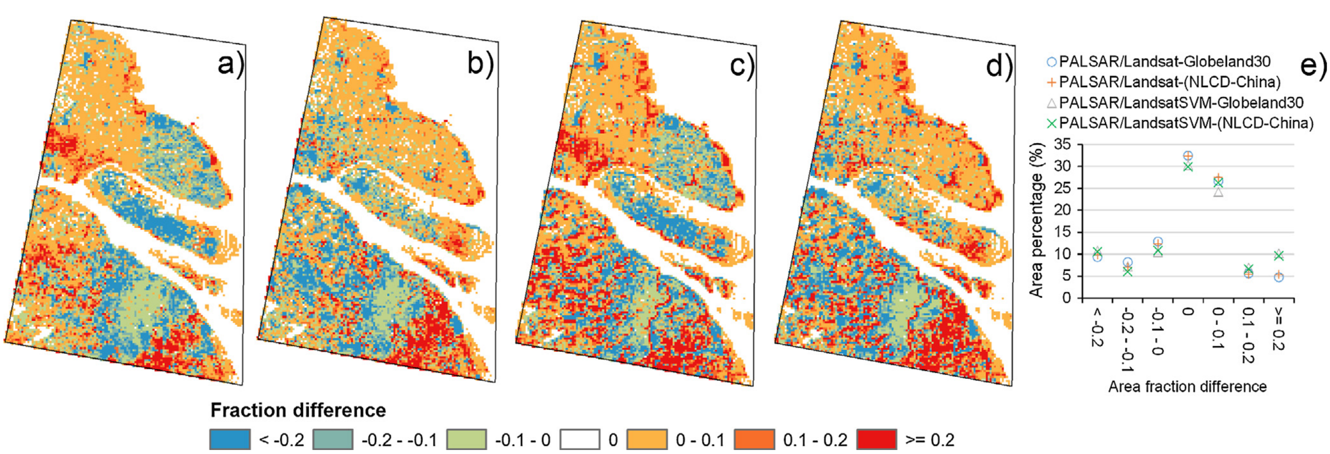

Fig. 13. Spatial differences between built-up maps and impervious surface maps at the spatial resolution of 1-km in 2010. The difference between PALSAR/Landsat built-up map and Globeland30 (a) and NLCD-China (b) impervious surface maps. The difference between PALSAR/Landsat$_{SVM}$ built-up map and Globeland30 (c) and NLCD-China (d) impervious surface maps. (e) is the area histogram distribution of (a–d).

(3167 km^2) are larger than PALSAR/Landsat built-up area (2805 km^2) and similar to PALSAR/Landsat$_{SVM}$ built-up area (3152 km^2). Significant linear relationships exist between PALSAR/Landsat and PALSAR/Landsat$_{SVM}$ built-up maps and the Globeland30 and NLCD-China impervious surface maps (Fig. 12e–h). At the 1-km pixel scale, the areas of GlobeLand30 and NLCD-China impervious surface were about 105% and 105% of the area of PALSAR/Landsat built-up, and about 98% and 99% of the area of PALSAR/Landsat$_{SVM}$ built-up, respectively.

In the urban core, the area fraction of the built-up map was reasonably lower (~0.1) than those of impervious surface maps (Fig. 13). In the peri-urban and rural area, the area fraction of PALSAR/Landsat$_{SVM}$ built-up maps had relatively larger estimation ($\geqslant$0.2) than those of impervious surface maps in about 10% of the total area, while only about 5% for the PALSAR/Landsat built-up map (Fig. 13). The spatial comparison between our built-up map and the impervious surface maps clearly provide insight for the improvement of the impervious surface maps in the future.

4.3. Potential of our pixel- and rule-based decision tree approach for identifying and mapping built-up area

Recent studies have been focusing on urban and impervious surface expansion and their impacts on carbon emission (Seto et al., 2012), biodiversity loss (Guneralp and Seto, 2013; Seto et al., 2012) and climate change (Kalnay and Cai, 2003; Miao et al., 2011; Weng et al., 2011; Zhang et al., 2009). However, the area, spatial distribution and density information of built-up along urban-rural areas have been hardly investigated. The pixel-based decision tree approach proposed in this study has the potential to map built-up in both urban and rural settings at the spatial resolution of 30 m, which enables people to investigate the spatial patterns of built-up in the urban/rural landscapes. Accurate built-up maps could be used to estimate population density in different communities. Use of these maps could help to investigate their pressure on the environment, which will deepen our understandings about effects of human activities on both climate and global environment change (He et al., 2014; IPCC, 2007; Kalnay and Cai, 2003; Sellers et al., 1997).

From the perspective of optical remote sensing, built-up in urban cores are often difficult to distinguish from barren land and sparse vegetation classes, while built-up in peri-urban and rural areas are easily confused with vegetation classes (Friedl et al., 2010). We extended the identification features for built-up from spectral space to both spectral and structure spaces. PALSAR HH gamma-naught and Landsat $NDVI_{max}$ presented stable and similar features for built-up over years, even though they were acquired in different months (Fig. 7). The potential of their combination was proven for built-up identification in the Yangtze River Delta. Based on the literature review, urban areas showed similar features of PALSAR HH backscatter in different climate regions, including boreal zone (Lonnqvist et al., 2010; Thiel et al., 2009), temperate zone (this study), subtropical zone (Chen et al., 2016) and tropical zone (Dong et al., 2012; Qin et al., 2015), respectively. Similar and slightly different thresholds from greenness ($NDVI_{max}$) and structure (HH gamma-naught) are expected to be effective for identifying and mapping built-up in other regions.

In this study, the 30-m Landsat and ALOS PALSAR imagery works well for large patches of built-up but has limited ability to map small and scattered built-up in rural areas (Fig. 9). Finer spatial resolution imagery is needed to refine these mixed pixels and further calibrate the built-up maps. 10-m spatial resolution images would be suitable for mapping built-up in the complex urban-rural landscape (Lu et al., 2011b), such as Sentinel-2 multispectral images and ALOS-2 PALSAR-2 Fine model L-band images.

5. Conclusions

Accurate estimation of the area, spatial distribution, and the density of regional built-up are fundamental information for human settlement design, planning, and management. We proposed a novel approach to map spatial and temporal patterns of built-up through the integration of 30-m Landsat and 25-m ALOS PALSAR imagery. We used a combination of structure, greenness and water coverage information to map built-up area. The results showed that the proposed pixel- and rule-based decision tree approach can identify built-up area reasonably well in both urban and rural areas from 2007 to 2010, and improvement was achieved over image-based SVM approach. The average annual increase of built-up areas was about 80 km^2 per year. The built-up maps could refine current impervious surface products generated by optical images and prompt their improvement. The application of this proposed approach in large regions needs further validation, including additional case studies in hotspots of urbanization across the world. Annual built-up maps at fine spatial resolutions are needed for better understanding the interaction between human activities and natural ecosystems.

Acknowledgements

This study was supported in part by research grants from the National Aeronautics and Space Administration (NASA) Land Cover and Land Use Change program (NNX11AJ35G and NNX14AD78G), National Science Foundation (NSF) EPSCoR program (OIA-1301789), and National Institutes of Health (NIH) (1R01AI101028-01A1). We thank three anonymous reviewers for their valuable comments to improve this study. We thank Sarah Xiao at Yale University and Brian A. Alikhani at the University of Oklahoma for English editing of the manuscript.

References

Bagan, H., Yamagata, Y., 2012. Landsat analysis of urban growth: how Tokyo became the world's largest megacity during the last 40 years. Remote Sens. Environ. 127, 210–222.
Ban, Y.F., Jacob, A., Gamba, P., 2015. Spaceborne SAR data for global urban mapping at 30 m resolution using a robust urban extractor. Isprs J. Photogram. Remote Sens. 103, 28–37.
Chen, B., Li, X., Xiao, X., Zhao, B., Dong, J., Kou, W., Qin, Y., Yang, C., Wu, Z., Sun, R., Lan, G., Xie, G., 2016. Mapping tropical forests and deciduous rubber plantations in Hainan Island, China by integrating PALSAR 25-m and multi-temporal Landsat images. Int. J. Appl. Earth Obs. Geoinf. 50, 117–130.
Chen, J., Chen, J., Liao, A.P., Cao, X., Chen, L.J., Chen, X.H., He, C.Y., Han, G., Peng, S., Lu, M., Zhang, W.W., Tong, X.H., Mills, J., 2015. Global land cover mapping at 30 m resolution: a POK-based operational approach. Isprs J. Photogram. Remote Sens. 103, 7–27.
Corbane, C., Faure, J.F., Baghdadi, N., Villeneuve, N., Petit, M., 2008. Rapid urban mapping using SAR/optical imagery synergy. Sensors 8, 7125–7143.
Dare, P.M., 2005. Shadow analysis in high-resolution satellite imagery of urban areas. Photogram. Eng. Remote Sens. 71, 169–177.
DeFries, R.S., Foley, J.A., Asner, G.P., 2004. Land-use choices: balancing human needs and ecosystem function. Front. Ecol. Environ. 2, 249–257.
Dong, J.W., Xiao, X.M., Kou, W.L., Qin, Y.W., Zhang, G.L., Li, L., Jin, C., Zhou, Y.T., Wang, J., Biradar, C., Liu, J.Y., Moore, B., 2015. Tracking the dynamics of paddy rice planting area in 1986–2010 through time series Landsat images and phenology-based algorithms. Remote Sens. Environ. 160, 99–113.
Dong, J.W., Xiao, X.M., Sheldon, S., Biradar, C., Duong, N.D., Hazarika, M., 2012. A comparison of forest cover maps in Mainland Southeast Asia from multiple sources: PALSAR, MERIS, MODIS and FRA. Remote Sens. Environ. 127, 60–73.
Esch, T., Marconcini, M., Felbier, A., Roth, A., Heldens, W., Huber, M., Schwinger, M., Taubenbock, H., Muller, A., Dech, S., 2013. Urban footprint processor-fully automated processing chain generating settlement masks from global data of the TanDEM-X Mission. IEEE Geosci. Remote Sens. Lett. 10, 1617–1621.
Esch, T., Thiel, M., Schenk, A., Roth, A., Muller, A., Dech, S., 2010. Delineation of urban footprints from TerraSAR-X data by analyzing speckle characteristics and intensity information. IEEE Trans. Geosci. Remote Sens. 48, 905–916.
Florczyk, A.J., Ferri, S., Syrris, V., Kemper, T., Halkia, M., Soille, P., Pesaresi, M., 2016. A new European settlement map from optical remotely sensed data. Ieee J. Select. Top. Appl. Earth Observ. Remote Sens. 9, 1978–1992.
Friedl, M.A., Brodley, C.E., 1997. Decision tree classification of land cover from remotely sensed data. Remote Sens. Environ. 61, 399–409.
Friedl, M.A., Sulla-Menashe, D., Tan, B., Schneider, A., Ramankutty, N., Sibley, A., Huang, X.M., 2010. MODIS Collection 5 global land cover: algorithm refinements and characterization of new datasets. Remote Sens. Environ. 114, 168–182.
Gamba, P., Aldrighi, M., Stasolla, M., 2011. Robust extraction of urban area extents in HR and VHR SAR images. Ieee J. Select. Top. Appl. Earth Observ. Remote Sens. 4, 27–34.
Gamon, J.A., Field, C.B., Goulden, M.L., Griffin, K.L., Hartley, A.E., Joel, G., Penuelas, J., Valentini, R., 1995. Relationships between Ndvi, Canopy Structure, and Photosynthesis in 3 Californian Vegetation Types. Ecol. Appl. 5, 28–41.
Gao, F., De Colstoun, E.B., Ma, R.H., Weng, Q.H., Masek, J.G., Chen, J., Pan, Y.Z., Song, C. H., 2012. Mapping impervious surface expansion using medium-resolution satellite image time series: a case study in the Yangtze River Delta, China. Int. J. Remote Sens. 33, 7609–7628.
Gong, P., Liang, S., Carlton, E.J., Jiang, Q.W., Wu, J.Y., Wang, L., Remais, J.V., 2012. Urbanisation and health in China. Lancet 379, 843–852.

Goodwin, N.R., Collett, L.J., Denham, R.J., Flood, N., Tindall, D., 2013. Cloud and cloud shadow screening across Queensland, Australia: an automated method for Landsat TM/ETM plus time series. Remote Sens. Environ. 134, 50–65.
Guneralp, B., Seto, K.C., 2013. Futures of global urban expansion: uncertainties and implications for biodiversity conservation. Environ. Res. Lett. 8.
Hall, D.K., Riggs, G.A., Salomonson, V.V., 1995. Development of methods for mapping global snow cover using moderate resolution imaging spectroradiometer data. Remote Sens. Environ. 54, 127–140.
Hall, D.K., Riggs, G.A., Salomonson, V.V., DiGirolamo, N.E., Bayr, K.J., 2002. MODIS snow-cover products. Remote Sens. Environ. 83, 181–194.
He, C.Y., Liu, Z.F., Tian, J., Ma, Q., 2014. Urban expansion dynamics and natural habitat loss in China: a multiscale landscape perspective. Glob. Change Biol. 20, 2886–2902.
Hsieh, P.F., Lee, L.C., Chen, N.Y., 2001. Effect of spatial resolution on classification errors of pure and mixed pixels in remote sensing. IEEE Trans. Geosci. Remote Sens. 39, 2657–2663.
Hu, X.F., Weng, Q.H., 2011. Impervious surface area extraction from IKONOS imagery using an object-based fuzzy method. Geocarto Int. 26, 3–20.
Huete, A., Didan, K., Miura, T., Rodriguez, E.P., Gao, X., Ferreira, L.G., 2002. Overview of the radiometric and biophysical performance of the MODIS vegetation indices. Remote Sens. Environ. 83, 195–213.
Huete, A.R., Liu, H.Q., Batchily, K., vanLeeuwen, W., 1997. A comparison of vegetation indices global set of TM images for EOS-MODIS. Remote Sens. Environ. 59, 440–451.
IPCC, 2007. Climate Change 2007: The Physical Science Basis. Cambridge University Press, Cambridge, United Kingdom and New York, NY, USA.
Jiao, T., Liu, R.G., Liu, Y., Pisek, J., Chen, J.M., 2014. Mapping global seasonal forest background reflectivity with Multi-angle Imaging Spectroradiometer data. J. Geophys. Res.-Biogeosci. 119, 1063–1077.
Kalnay, E., Cai, M., 2003. Impact of urbanization and land-use change on climate. Nature 423, 528–531.
Kuang, W.H., Chi, W.F., Lu, D.S., Dou, Y.Y., 2014. A comparative analysis of megacity expansions in China and the U.S.: Patterns, rates and driving forces. Landscape Urban Plan. 132, 121–135.
Kuang, W.H., Liu, J.Y., Dong, J.W., Chi, W.F., Zhang, C., 2016. The rapid and massive urban and industrial land expansions in China between 1990 and 2010: a CLUD-based analysis of their trajectories, patterns, and drivers. Landscape Urban Plan. 145, 21–33.
Kuang, W.H., Liu, J.Y., Zhang, Z.X., Lu, D.S., Xiang, B., 2013. Spatiotemporal dynamics of impervious surface areas across China during the early 21st century. Chin. Sci. Bull. 58, 1691–1701.
Li, X., Gong, P., Liang, L., 2015. A 30-year (1984–2013) record of annual urban dynamics of Beijing City derived from Landsat data. Remote Sens. Environ. 166, 78–90.
Liu, J.Y., Kuang, W.H., Zhang, Z.X., Xu, X.L., Qin, Y.W., Ning, J., Zhou, W.C., Zhang, S. W., Li, R.D., Yan, C.Z., Wu, S.X., Shi, X.Z., Jiang, N., Yu, D.S., Pan, X.Z., CHi, W.F., 2014. Spatiotemporal characteristics, patterns, and causes of land-use changes in China since the late 1980s. J. Geog. Sci. 24, 195–210.
Liu, Z.F., He, C.Y., Zhang, Q.F., Huang, Q.X., Yang, Y., 2012. Extracting the dynamics of urban expansion in China using DMSP-OLS nighttime light data from 1992 to 2008. Landscape Urban Plan. 106, 62–72.
Lonnqvist, A., Rauste, Y., Molinier, M., Hame, T., 2010. Polarimetric SAR data in land cover mapping in boreal zone. IEEE Trans. Geosci. Remote Sens. 48, 3652–3662.
Lu, D.S., Hetrick, S., Moran, E., 2011a. Impervious surface mapping with Quickbird imagery. Int. J. Remote Sens. 32, 2519–2533.
Lu, D.S., Li, G.Y., Kuang, W.H., Moran, E., 2014. Methods to extract impervious surface areas from satellite images. Int. J. Digital Earth 7, 93–112.
Lu, D.S., Li, G.Y., Moran, E., Batistella, M., Freitas, C.C., 2011b. Mapping impervious surfaces with the integrated use of Landsat Thematic Mapper and radar data: a case study in an urban-rural landscape in the Brazilian Amazon. Isprs J. Photogram. Remote Sens. 66, 798–808.
Lu, D.S., Weng, Q.H., 2006. Use of impervious surface in urban land-use classification. Remote Sens. Environ. 102, 146–160.
Lu, D.S., Weng, Q.H., 2009. Extraction of urban impervious surfaces from an IKONOS image. Int. J. Remote Sens. 30, 1297–1311.
Ma, J., Ma, J., 2014. Shanghai Statistical Yearbook. Bureau of Shanghai Statistics.
Masek, J.G., Vermote, E.F., Saleous, N.E., Wolfe, R., Hall, F.G., Huemmrich, K.F., Gao, F., Kutler, J., Lim, T.K., 2006. A Landsat surface reflectance dataset for North America, 1990–2000. IEEE Geosci. Remote Sens. Lett. 3, 68–72.
Mertes, C.M., Schneider, A., Sulla-Menashe, D., Tatem, A.J., Tan, B., 2015. Detecting change in urban areas at continental scales with MODIS data. Remote Sens. Environ. 158, 331–347.
Miao, S.G., Chen, F., Li, Q.C., Fan, S.Y., 2011. Impacts of urban processes and urbanization on summer precipitation: a case study of heavy rainfall in Beijing on 1 August 2006. J. Appl. Meteorol. Climatol. 50, 806–825.
Myint, S.W., Gober, P., Brazel, A., Grossman-Clarke, S., Weng, Q.H., 2011. Per-pixel vs. object-based classification of urban land cover extraction using high spatial resolution imagery. Remote Sens. Environ. 115, 1145–1161.
Olofsson, P., Foody, G.M., Herold, M., Stehman, S.V., Woodcock, C.E., Wulder, M.A., 2014. Good practices for estimating area and assessing accuracy of land change. Remote Sens. Environ. 148, 42–57.
Pandey, B., Joshi, P.K., Seto, K.C., 2013. Monitoring urbanization dynamics in India using DMSP/OLS night time lights and SPOT-VGT data. Int. J. Appl. Earth Obs. Geoinf. 23, 49–61.
Pesaresi, M., Ehrlich, D., Caravaggi, I., Kauffmann, M., Louvrier, C., 2011. Toward global automatic built-up area recognition using optical VHR imagery. Ieee J. Select. Top. Appl. Earth Observ. Remote Sens. 4, 923–934.
Pesaresi, M., Gerhardinger, A., 2011. Improved textural built-up presence index for automatic recognition of human settlements in arid regions with scattered vegetation. Ieee J. Select. Top. Appl. Earth Observ. Remote Sens. 4, 16–26.
Pesaresi, M., Gerhardinger, A., Kayitakire, F., 2008. A robust built-up area presence index by anisotropic rotation-invariant textural measure. Ieee J. Select. Top. Appl. Earth Observ. Remote Sens. 1, 180–192.
Pesaresi, M., Guo, H.D., Blaes, X., Ehrlich, D., Ferri, S., Gueguen, L., Halkia, M., Kauffmann, M., Kemper, T., Lu, L.L., Marin-Herrera, M.A., Ouzounis, G.K., Scavazzon, M., Soille, P., Syrris, V., Zanchetta, L., 2013. A global human settlement layer from optical HR/VHR RS data: concept and first results. Ieee J. Select. Top. Appl. Earth Observ. Remote Sens. 6, 2102–2131.
Qin, Y., Xiao, X., Dong, J., Zhang, G., Shimada, M., Liu, J., Li, C., Kou, W., Moore Iii, B., 2015. Forest cover maps of China in 2010 from multiple approaches and data sources: PALSAR, Landsat, MODIS, FRA, and NFI. Isprs J. Photogram. Remote Sens. 109, 1–16.
Rouse, J.W., Haas, R.H., Schell, J.A., Deering, D.W., 1974. Monitoring vegetation systems in the great plains with Erts, Greenbelt: NASA SP-351. In: Third Earth Resources Technology Satellite-1 Symposium, pp. 3100–3017.
Schneider, A., Friedl, M.A., Potere, D., 2009. A new map of global urban extent from MODIS satellite data. Environ. Res. Lett. 4.
Schneider, A., Friedl, M.A., Potere, D., 2010. Mapping global urban areas using MODIS 500-m data: new methods and datasets based on 'urban ecoregions'. Remote Sens. Environ. 114, 1733–1746.
Schneider, A., Mertes, C.M., 2014. Expansion and growth in Chinese cities, 1978-2010. Environm. Res. Lett. 9.
Schneider, A., Mertes, C.M., Tatem, A.J., Tan, B., Sulla-Menashe, D., Graves, S.J., Patel, N.N., Horton, J.A., Gaughan, A.E., Rollo, J.T., Schelly, I.H., Stevens, F.R., Dastur, A., 2015. A new urban landscape in East-Southeast Asia, 2000-2010. Environ. Res. Lett. 10.
Sellers, P.J., Dickinson, R.E., Randall, D.A., Betts, A.K., Hall, F.G., Berry, J.A., Collatz, G. J., Denning, A.S., Mooney, H.A., Nobre, C.A., Sato, N., Field, C.B., Henderson-Sellers, A., 1997. Modeling the exchanges of energy, water, and carbon between continents and the atmosphere. Science 275, 502–509.
Seto, K.C., Guneralp, B., Hutyra, L.R., 2012. Global forecasts of urban expansion to 2030 and direct impacts on biodiversity and carbon pools. Proc. Natl. Acad. Sci. U.S.A. 109, 16083–16088.
Shimada, M., Isoguchi, O., Tadono, T., Isono, K., 2009. PALSAR radiometric and geometric calibration. IEEE Trans. Geosci. Remote Sens. 47, 3915–3932.
Shimada, M., Itoh, T., Motooka, T., Watanabe, M., Shiraishi, T., Thapa, R., Lucas, R., 2014. New global forest/non-forest maps from ALOS PALSAR data (2007–2010). Remote Sens. Environ. 155, 13–31.
Singh, K.K., Vogler, J.B., Shoemaker, D.A., Meentemeyer, R.K., 2012. LiDAR-Landsat data fusion for large-area assessment of urban land cover: balancing spatial resolution, data volume and mapping accuracy. Isprs J. Photogram. Remote Sens. 74, 110–121.
Small, C., 2005. A global analysis of urban reflectance. Int. J. Remote Sens. 26, 661–681.
Suykens, J.A.K., Horvath, G., Basu, S., Micchelli, C., Vandewalle, J., (Eds), 2003. Advances in Learning Theory: Methods, Models and Applications. IOS Press.
Syrris, V., Ferri, S., Ehrlich, D., Pesaresi, M., 2015. Image enhancement and feature extraction based on low-resolution satellite data. Ieee J. Select. Top. Appl. Earth Observ. Remote Sens. 8, 1986–1995.
Taubenbock, H., Esch, T., Felbier, A., Roth, A., Dech, S., 2011. Pattern-based accuracy assessment of an urban footprint classification using TerraSAR-X data. IEEE Geosci. Remote Sens. Lett. 8, 278–282.
Thiel, C.J., Thiel, C., Schmullius, C.C., 2009. Operational large-area forest monitoring in Siberia using ALOS PALSAR summer intensities and winter coherence. IEEE Trans. Geosci. Remote Sens. 47, 3993–4000.
Turner, D.P., Cohen, W.B., Kennedy, R.E., Fassnacht, K.S., Briggs, J.M., 1999. Relationships between leaf area index and Landsat TM spectral vegetation indices across three temperate zone sites. Remote Sens. Environ. 70, 52–68.
Vermote, E.F., ElSaleous, N., Justice, C.O., Kaufman, Y.J., Privette, J.L., Remer, L., Roger, J.C., Tanre, D., 1997. Atmospheric correction of visible to middle-infrared EOS-MODIS data over land surfaces: background, operational algorithm and validation. J. Geophys. Res.-Atmos. 102, 17131–17141.
Voltersen, M., Berger, C., Hese, S., Schmullius, C., 2014. Object-based land cover mapping and comprehensive feature calculation for an automated derivation of urban structure types at block level. Remote Sens. Environ. 154, 192–201.
Weng, Q.H., 2012. Remote sensing of impervious surfaces in the urban areas: requirements, methods, and trends. Remote Sens. Environ. 117, 34–49.
Weng, Q.H., Hu, X.F., Liu, H., 2009. Estimating impervious surfaces using linear spectral mixture analysis with multitemporal ASTER images. Int. J. Remote Sens. 30, 4807–4830.
Weng, Q.H., Hu, X.F., Lu, D.S., 2008. Extracting impervious surfaces from medium spatial resolution multispectral and hyperspectral imagery: a comparison. Int. J. Remote Sens. 29, 3209–3232.
Weng, Q.H., Rajasekar, U., Hu, X.F., 2011. Modeling urban heat islands and their relationship with impervious surface and vegetation abundance by using ASTER images. IEEE Trans. Geosci. Remote Sens. 49, 4080–4089.
Xian, G., Homer, C., 2010. Updating the 2001 national land cover database impervious surface products to 2006 using landsat imagery change detection methods. Remote Sens. Environ. 114, 1676–1686.

Xiao, X., Boles, S., Frolking, S., Salas, W., Moore, B., Li, C., He, L., Zhao, R., 2002a. Landscape-scale characterization of cropland in China using Vegetation and landsat TM images. Int. J. Remote Sens. 23, 3579–3594.
Xiao, X., Boles, S., Frolking, S., Salas, W., Moore, B., Li, C., He, L., Zhao, R., 2002b. Observation of flooding and rice transplanting of paddy rice fields at the site to landscape scales in China using VEGETATION sensor data. Int. J. Remote Sens. 23, 3009–3022.
Xiao, X.M., Boles, S., Frolking, S., Li, C.S., Babu, J.Y., Salas, W., Moore, B., 2006. Mapping paddy rice agriculture in South and Southeast Asia using multi-temporal MODIS images. Remote Sens. Environ. 100, 95–113.
Xiao, X.M., Boles, S., Liu, J.Y., Zhuang, D.F., Frolking, S., Li, C.S., Salas, W., Moore, B., 2005. Mapping paddy rice agriculture in southern China using multi-temporal MODIS images. Remote Sens. Environ. 95, 480–492.
Xie, Y., Weng, Q., 2016. Updating urban extents with nighttime light imagery by using an object-based thresholding method. Remote Sens. Environ. 187, 1–13.
Yin, J., Yin, Z.E., Zhong, H.D., Xu, S.Y., Hu, X.M., Wang, J., Wu, J.P., 2011. Monitoring urban expansion and land use/land cover changes of Shanghai metropolitan area during the transitional economy (1979–2009) in China. Environ. Monit. Assess. 177, 609–621.
Yu, B.L., Liu, H.X., Wu, J.P., Hu, Y.J., Zhang, L., 2010. Automated derivation of urban building density information using airborne LiDAR data and object-based method. Landscape Urban Plan. 98, 210–219.
Zha, Y., Gao, J., Ni, S., 2003. Use of normalized difference built-up index in automatically mapping urban areas from TM imagery. Int. J. Remote Sens. 24, 583–594.
Zhang, C.L., Chen, F., Miao, S.G., Li, Q.C., Xia, X.A., Xuan, C.Y., 2009. Impacts of urban expansion and future green planting on summer precipitation in the Beijing metropolitan area. J. Geophys. Res.-Atmos. 114.
Zhang, H.S., Lin, H., Li, Y., Zhang, Y.Z., Fang, C.Y., 2016. Mapping urban impervious surface with dual-polarimetric SAR data: an improved method. Landscape Urban Plan. 151, 55–63.
Zhang, L., Weng, Q.H., 2016. Annual dynamics of impervious surface in the Pearl River Delta, China, from 1988 to 2013, using time series Landsat imagery. Isprs J. Photogram. Remote Sens. 113, 86–96.
Zhang, Q.L., Seto, K.C., 2011. Mapping urbanization dynamics at regional and global scales using multi-temporal DMSP/OLS nighttime light data. Remote Sens. Environ. 115, 2320–2329.
Zhang, Y., Wang, C.Z., Chen, X., Su, S.L., 2011. Support vector machine approach to identifying buildings using multi-temporal ALOS/PALSAR data. Int. J. Remote Sens. 32, 7163–7177.
Zhang, Y.Z., Zhang, H.S., Lin, H., 2014a. Improving the impervious surface estimation with combined use of optical and SAR remote sensing images. Remote Sens. Environ. 141, 155–167.
Zhang, Z.X., Wang, X., Zhao, X.L., Liu, B., Yi, L., Zuo, L.J., Wen, Q.K., Liu, F., Xu, J.Y., Hu, S.G., 2014b. A 2010 update of National Land Use/Cover Database of China at 1:100000 scale using medium spatial resolution satellite images. Remote Sens. Environ. 149, 142–154.
Zhou, Y.Y., Smith, S.J., Elvidge, C.D., Zhao, K.G., Thomson, A., Imhoff, M., 2014. A cluster-based method to map urban area from DMSP/OLS nightlights. Remote Sens. Environ. 147, 173–185.
Zhu, Z., Woodcock, C.E., 2012. Object-based cloud and cloud shadow detection in Landsat imagery. Remote Sens. Environ. 118, 83–94.
Zhu, Z., Woodcock, C.E., Rogan, J., Kellndorfer, J., 2012. Assessment of spectral, polarimetric, temporal, and spatial dimensions for urban and peri-urban land cover classification using Landsat and SAR data. Remote Sens. Environ. 117, 72–82.